ARTICLE

https://doi.org/10.1038/s41586-019-1295-z

Structural mechanism for NEK7-licensed activation of NLRP3 inflammasome

Humayun Sharif[1,2,9], Li Wang[1,2,9], Wei Li Wang[1,2,3,4,5,6,7,9], Venkat Giri Magupalli[1,2], Liudmila Andreeva[1,2], Qi Qiao[1,2], Arthur V. Hauenstein[1,2], Zhaolong Wu[3,4], Gabriel Núñez[8], Youdong Mao[3,4,5,6,7]* & Hao Wu[1,2]*

The NLRP3 inflammasome can be activated by stimuli that include nigericin, uric acid crystals, amyloid-β fibrils and extracellular ATP. The mitotic kinase NEK7 licenses the assembly and activation of the NLRP3 inflammasome in interphase. Here we report a cryo-electron microscopy structure of inactive human NLRP3 in complex with NEK7, at a resolution of 3.8 Å. The earring-shaped NLRP3 consists of curved leucine-rich-repeat and globular NACHT domains, and the C-terminal lobe of NEK7 nestles against both NLRP3 domains. Structural recognition between NLRP3 and NEK7 is confirmed by mutagenesis both in vitro and in cells. Modelling of an active NLRP3–NEK7 conformation based on the NLRC4 inflammasome predicts an additional contact between an NLRP3-bound NEK7 and a neighbouring NLRP3. Mutations to this interface abolish the ability of NEK7 or NLRP3 to rescue NLRP3 activation in NEK7-knockout or NLRP3-knockout cells. These data suggest that NEK7 bridges adjacent NLRP3 subunits with bipartite interactions to mediate the activation of the NLRP3 inflammasome.

Inflammasomes are cytoplasmic supramolecular complexes that form in response to exogenous microbial invasions and endogenous damage signals[1–3]. Inflammasomes activate inflammatory caspases such as caspase-1, which processes the proinflammatory cytokines interleukin 1β (IL-1β) and IL-18 for their maturation, and cleaves gasdermin D to generate the N-terminal fragment to induce pore formation, cytokine release and pyroptotic cell death[2,4,5]. NLRP3 belongs to the family of nucleotide-binding domain (NBD) and leucine-rich repeat (LRR)-containing proteins (NLRs). It has an N-terminal pyrin domain, which interacts with the adaptor protein ASC via interactions between pyrin domains; a central adenosine triphosphatase (ATPase) domain known as NACHT, which comprises an NBD, helical domain 1 (HD1), winged helix domain (WHD) and helical domain 2 (HD2); and a C-terminal LRR domain[6] (Fig. 1a). ASC also has a caspase recruitment domain, which recruits caspase-1 via interactions between the caspase recruitment domains, to promote caspase dimerization and activation. Previous studies have revealed that the pyrin and caspase recruitment domains both form filamentous assemblies through nucleated polymerization[7–9]. NLRP3 is an extensively studied inflammasome sensor activated by a spectrum of seemingly unrelated stimuli via induction of K^+ efflux[1–3,10–12]. Autosomal-dominant mutations of the *NLRP3* gene are related to autoinflammatory diseases that are collectively known as cryopyrin-associated periodic syndromes (CAPS); NLRP3 hyperactivation is directly connected to systematic and joint inflammation[1–3,10]. The mitotic Ser/Thr kinase NEK7 has recently been identified as an important requirement in NLRP3 activation via direct NLRP3–NEK7 interaction[13–16]. Because of its interaction with NEK9 during mitosis, and its limited quantity in cells, NEK7 licenses NLRP3 activation only in interphase[16]. However, the molecular mechanism of the NLRP3–NEK7 interaction remains unknown.

Cryo-electron microscopy structure determination

We expressed and purified a recombinant complex of maltose-binding protein (MBP)-tagged NLRP3 with the pyrin domains deleted (NLRP3Δ) and NEK7. Microscale thermophoresis showed a dissociation constant of 78.9 ± 38.5 nM between NLRP3 and NEK7 (Fig. 1b, Extended Data Fig. 1a). A thermal shift assay indicated that the NLRP3 inhibitor MCC950[17] and ADP both increased the stability of NLRP3 or of the complex, but not of NEK7 alone (Extended Data Fig. 1b–d). However, cryo-electron microscopy (cryo-EM) images of the complex showed poor contrast, probably owing to the relatively small size of the complex (about 185 kDa with the MBP tag).

To facilitate structure determination, we generated an artificial NEK7 dimer that was based on a dimer structure of protein kinase R (RCSB Protein Data Bank (PDB) code 2A19)[18] (Extended Data Fig. 1e). The engineered NEK7 formed a dimeric complex with NLRP3, as shown by a shift in the elution position from a gel filtration column and by multi-angle light scattering measurements (Fig. 1c, d, Extended Data Fig. 1f). Although dimeric in solution, 2D classification revealed mostly monomeric NLRP3–NEK7 particles, which suggests that the two complexes in the dimer are flexibly linked. We speculate that, despite the flexibility, the larger dimer complexes facilitated particle-picking and 3D reconstruction. Cryo-EM analysis was first conducted using a Talos Arctica microscope, which resulted in a 4.3 Å reconstruction (Extended Data Fig. 2a–d, Extended Data Table 1). A larger cryo-EM dataset that contained 15,681 movies collected on a Titan Krios microscope (Extended Data Fig. 2e) gave rise to the final 3.8 Å map, refined with 108,771 particles selected from multiple rounds of 2D and 3D classifications (Fig. 1e, f, Extended Data Fig. 2e–g, Extended Data Table 1). The data included 1,340 movies collected at a stage tilt of 20°, which improved particle orientation distribution (Extended Data Fig. 2f).

Atomic model building was initially performed on the 4.3 Å map, assisted by structures of other NLRs and NEK7, and was finalized on

[1]Department of Biological Chemistry and Molecular Pharmacology, Harvard Medical School, Boston, MA, USA. [2]Program in Cellular and Molecular Medicine, Boston Children's Hospital, Boston, MA, USA. [3]State Key Laboratory for Artificial Microstructures and Mesoscopic Physics, School of Physics, Peking University, Beijing, China. [4]Center for Quantitative Biology, Peking University, Beijing, China. [5]Intel Parallel Computing Center for Structural Biology, Dana-Farber Cancer Institute, Boston, MA, USA. [6]Department of Cancer Immunology and Virology, Dana-Farber Cancer Institute, Boston, MA, USA. [7]Department of Microbiology, Harvard Medical School, Boston, MA, USA. [8]Department of Pathology and Comprehensive Cancer Center, University of Michigan Medical School, Ann Arbor, MI, USA. [9]These authors contributed equally: Humayun Sharif, Li Wang, Wei Li Wang. *e-mail: ymao@pku.edu.cn; wu@crystal.harvard.edu

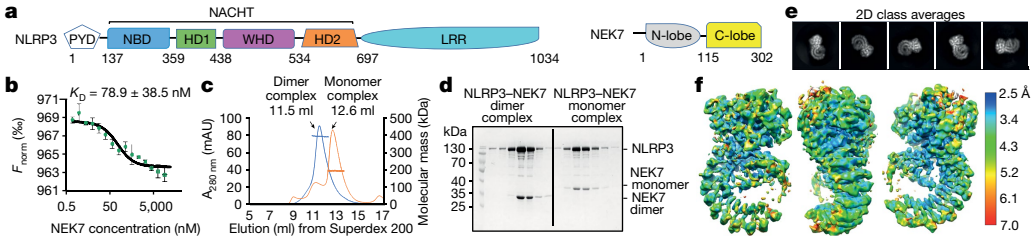

Fig. 1 | Biochemical characterization and cryo-EM structure determination. a, Schematic domain representation of human NLRP3 and NEK7, with labelled domain boundary defined from this work. PYD, pyrin domain. **b**, Microscale thermophoresis analysis of NEK7 binding to NLRP3. A dissociation constant of 78.9 ± 38.5 nM was calculated from three independent replicates (shown as mean ± s.d.). **c**, Reconstitution of NLRP3–NEK7 dimer and monomer complexes on Superdex 200 gel filtration column (repeated ≥ 5 times). Molecular mass distribution within each peak was calculated from in-line multi-angle light scattering measurements, and is shown in blue and orange for the dimer and monomer complexes, respectively (performed once). mAU, milli-absorbance units. **d**, SDS–PAGE gels of eluted fractions of dimer and monomer complexes (repeated ≥ 5 times). **e**, Representative 2D class averages from the 300 keV cryo-EM dataset, selected amongst 100 classes. **f**, The final cryo-EM density map (shown at 6σ) in three orientations and coloured with local resolutions by ResMap[41].

the 3.8 Å map (Fig. 2a, Extended Data Fig. 3). The map revealed an earring shape—which is characteristic of NLRs, such as NLRC4[6,19,20], NOD2[21] and NAIP5[22,23]—that contains a curved LRR domain and a compact NACHT that comprises an NBD, HD1, WHD and HD2 (Fig. 2a). The LRR region comprises 12 repeats, consistent with the structure prediction using Phyre2[24] (Extended Data Fig. 4). The density encircled by the LRR fit well with the C-terminal lobe of the crystal structure of human NEK7 (PDB code 2WQN)[25] as a rigid body. No density was visible for the N-terminal lobe of NEK7 (Extended Data Fig. 3a, h), probably because the mutations introduced to this region to generate a NEK7 dimer affected the structural integrity of NEK7 N-lobe.

Overall structure of the complex, and interactions

The final atomic model contains almost the entire NLRP3Δ (without the N-terminal MBP), the NEK7 C-lobe and the ADP bound to the NBD of NLRP3 (Fig. 2a, Extended Data Table 1, Supplementary Video 1). When the full-length NEK7 structure is overlaid with the NLRP3–NEK7 model, the N-lobe extends away from the complex with no steric hindrance against NLRP3 (Extended Data Fig. 5a). The activation loop, including S195 (the phosphorylation of which activates NEK7), is disordered in the NLRP3–NEK7 complex and does not contact NLRP3 (Extended Data Fig. 5b), which is consistent with the observation that both active and inactive NEK7 can support NLRP3 activation[13–15]. The NBD–HD1–WHD module of NLRP3 exhibits a conformation that is similar to the inactive conformation of NLRC4 and NOD2, whereas the HD2 and LRR structures are variable among known structures in the NLR family (Extended Data Fig. 5c–e). NEK7 binds an LRR region in which the phosphorylated S533 residue of NLRC4 HD2 interacts intramolecularly, although the role of S533 phosphorylation in NLRC4 activation remains controversial[6,26,27] (Extended Data Fig. 5e).

NLRP3 interacts with NEK7 at multiple surfaces, including the LRR, HD2 and NBD (Extended Data Figs. 6, 7). The calculated iso-electric points of NEK7 and NLRP3 are 8.5 and 6.2, respectively, which makes NEK7 positively charged overall, and NLRP3 negatively charged overall, at physiological pH (Fig. 2b). The NEK7 C-lobe is even more positively charged, with a calculated iso-electric point of 9.0. Indeed, the interaction between NLRP3 and NEK7 is dictated partly by electrostatic complementarity (Fig. 2b). The positively charged nature of NEK7 is also reflected in the bound SO_4 ion in its crystal structure[25], at its interface with NLRP3 (Extended Data Fig. 8a). The interactions between NLRP3 and NEK7 can be divided into two interfaces: those between the LRR of NLRP3 and the first half of the NEK7 C-lobe (Fig. 3a, b, Extended Data Fig. 8b) and those between NACHT (NBD and HD2) and the second half of the NEK7 C-lobe (Fig. 3a, c, Extended Data Fig. 8b). These interactions bury surface areas of about 880 Å^2 and about 770 Å^2, respectively.

Structural insights into NEK7 for NLRP3 interaction

On NEK7, residues with largest buried surface areas at the interface (as assessed by PISA[28]) include Q129, R131 and R136; these residues interact with the LRR domain of NLRP3 (Fig. 3b). R121, R131 and R136 also participate in hydrogen bonding or charged interactions. The NEK7 residues D261, E265 and E266 bury large surface areas at the interface with HD2 of NLRP3 (Fig. 3c, left). S260 and E266 also participate in hydrogen bonding or charged interactions at this interface. For the NBD interaction, the NEK7 residues D290, K293 and R294 appear to be the most extensive (Fig. 3c, right).

To deduce the importance of the observed contacts, we performed site-directed mutagenesis on NEK7 (Fig. 3d, e, Extended Data Figs. 6, 8c–e). The pulldown of SUMO-tagged wild-type and mutant NEK7 by MBP-tagged NLRP3 using amylose resin revealed that the most-marked effects came from mutations on Q129, R131 and R136 in the first half of the NEK7 C-lobe, all at the interface with the LRR of NLRP3 (interface I). The data explain previous immunoprecipitation results, in which a truncated NEK7 (amino acids 1–212, with the second half of the C-lobe removed) supported NLRP3 binding[13]. The residues S260, D261 and E265 of NEK7 for the HD2 interaction (interface II) also had substantial effects when they were mutated, whereas mutations

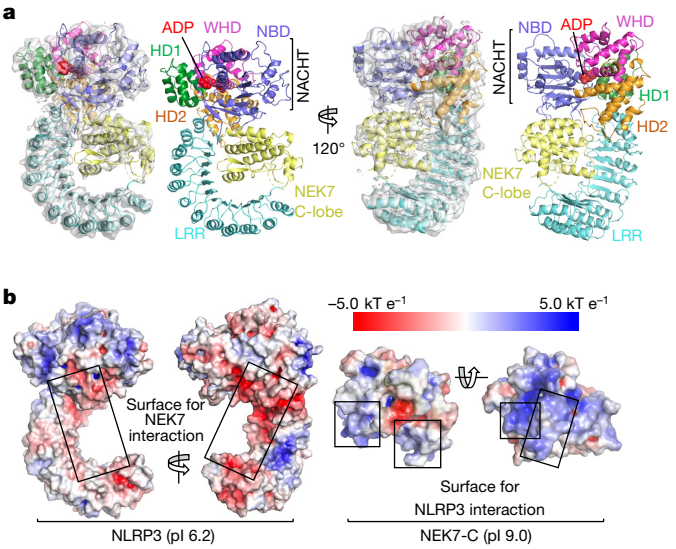

Fig. 2 | Cryo-EM structure overview. a, Ribbon diagrams of the complex, shown with and without the cryo-EM map (grey, 5σ) in two orientations. Domains are colour-coded as in Fig. 1a and the bound ADP is shown in sphere rendering. **b**, Electrostatic surface representation of NLRP3 and NEK7, colour-coded according to electrostatic potential from red (−5.0 kT e^{-1}, negatively charged) to blue (5.0 kT e^{-1}, positively charged). pI, iso-electric point.

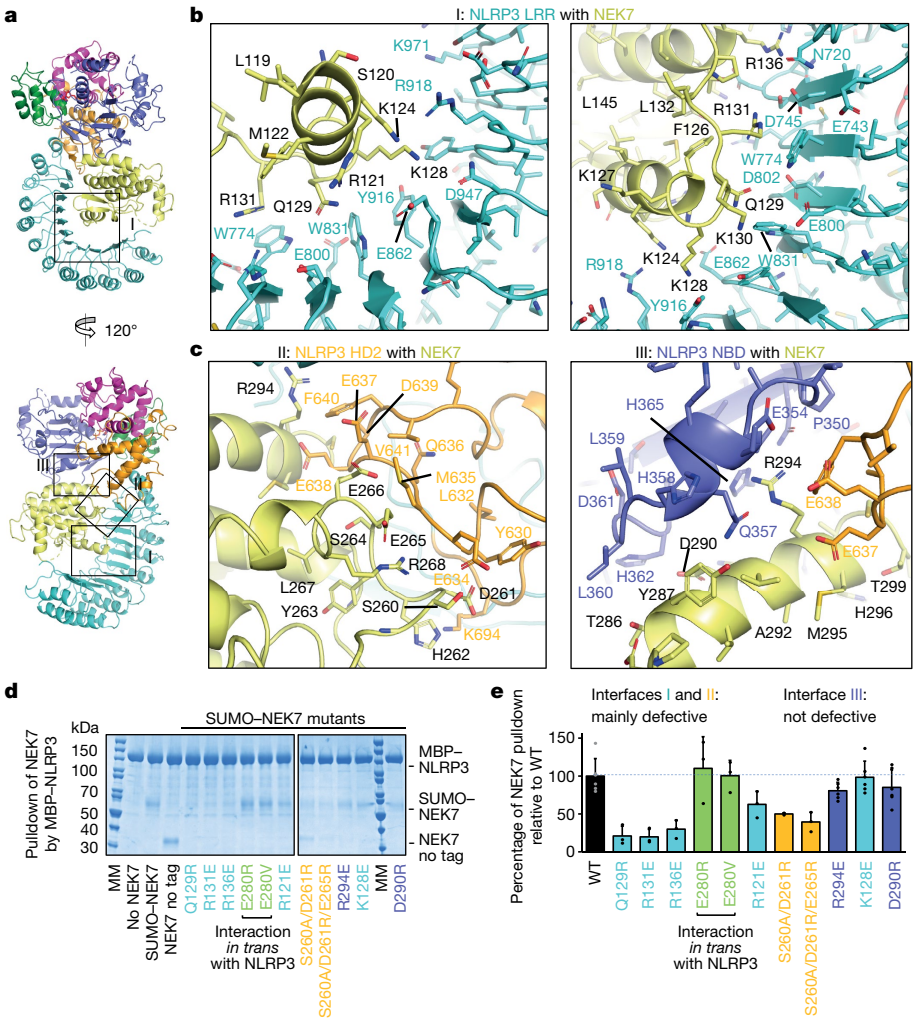

Fig. 3 | Structural insights into NEK7 interaction with NLRP3. a, The NLRP3–NEK7 complex in two orientations to denote the three interaction regions (I, II and III). **b**, **c**, Magnified views of interaction interfaces between NEK7 and LRR of NLRP3 (**b**) and between NEK7 and HD2 and NBD of NLRP3 (**c**), with main chains in cartoons and side chains in sticks. **d**, Pulldown of purified wild-type and mutant His-SUMO-tagged NEK7 by purified MBP-tagged wild-type NLRP3 using amylose resin. Experiments were performed between three and six times. NEK7 mutants are coloured by the domain of NLRP3 that they contact, as in **a**–**c**. MM, molecular mass markers. **e**, Quantification of mutant NEK7 binding to NLRP3 relative to wild-type (WT) NEK7 (shown as mean ± s.d., $n = 3$–6 replicates). Dots, individual data points. For gel source data, see Supplementary Fig. 1.

on NEK7 residues for the NBD interaction did not cause notable changes in NLRP3 interaction (Fig. 3d, e, Extended Data Figs. 6, 8c–e). Collectively, the mutagenesis data support the importance of interfaces I and II in the NLRP3–NEK7 interaction. Of note, the NLRP3 NBD no longer contacts NEK7 in a model of active NLRP3 based on the active NLRC4 conformation[19,20] (see below).

To further validate the observed NLRP3–NEK7 interface, we reconstituted wild-type and mutant NEK7 into NEK7-knockout immortalized mouse bone-marrow-derived macrophages (iBMDMs) and examined the response of the cells upon lipopolysaccharide (LPS) priming and nigericin treatment. Whereas wild-type NEK7 rescued NEK7-knockout iBMDMs in caspase-1 processing (Fig. 4a), IL-1β secretion (Fig. 4b) and cell death (Extended Data Fig. 8f), the NEK7 mutants were compromised in supporting nigericin-induced NLRP3 activation (Fig. 4a, b, Extended Data Fig. 8f).

Specificity and competition in NEK7–NLRP3 interaction

NEK6 is a kinase that is closely related to NEK7, with an overall 87% sequence identity in the kinase domain (Extended Data Fig. 6); however, it cannot support NLRP3 activation[13,14]. Sequence comparison among NEK proteins suggests that the main determinant of the specificity resides in the second part (residues 260–302) of the NEK7 C-lobe; the first part (residues 120–259) of the NEK7 C-lobe is largely conserved with NEK6 (Extended Data Fig. 6). Because both NEK proteins are involved in mitosis through an interaction with NEK9, we mapped the NEK9-binding site onto the NEK7 structure from the crystal structure of a NEK7–NEK9 complex[29] (Extended Data Fig. 8g). Consistent with the sequence conservation, the NEK9-binding site is mainly formed by the first part of the NEK7 C-lobe (Extended Data Fig. 8g), and partially overlaps with the NLRP3-binding site of NEK7 (Extended Data Fig. 8h). In addition, the back-to-back homodimer of NEK7 in the NEK7–NEK9 crystal structure[29] that is postulated for *trans*-autophosphorylation is incompatible with NLRP3 interaction (Extended Data Fig. 8i). We hypothesize that, once NEK7 binds NLRP3, it can no longer interact with NEK9 for mitosis, and vice versa. Therefore, it is not only the case that mitosis prevents NLRP3 inflammasome activation[14]—NLRP3 inflammasome activation may also prevent mitosis, when the quantity of NEK7 in macrophages is limited[14].

Structural insights into NLRP3 for NEK7 interaction

To test the functional relevance of NLRP3 residues that contact NEK7, we reconstituted wild-type and structure-based mutant NLRP3 into NLRP3-knockout iBMDMs and examined the response to NLRP3 stimulation. Upon LPS priming and nigericin treatment, wild-type reconstitution of NLRP3-knockout iBMDMs rescued the processing of caspase-1, as revealed by the appearance of the p20 large subunit

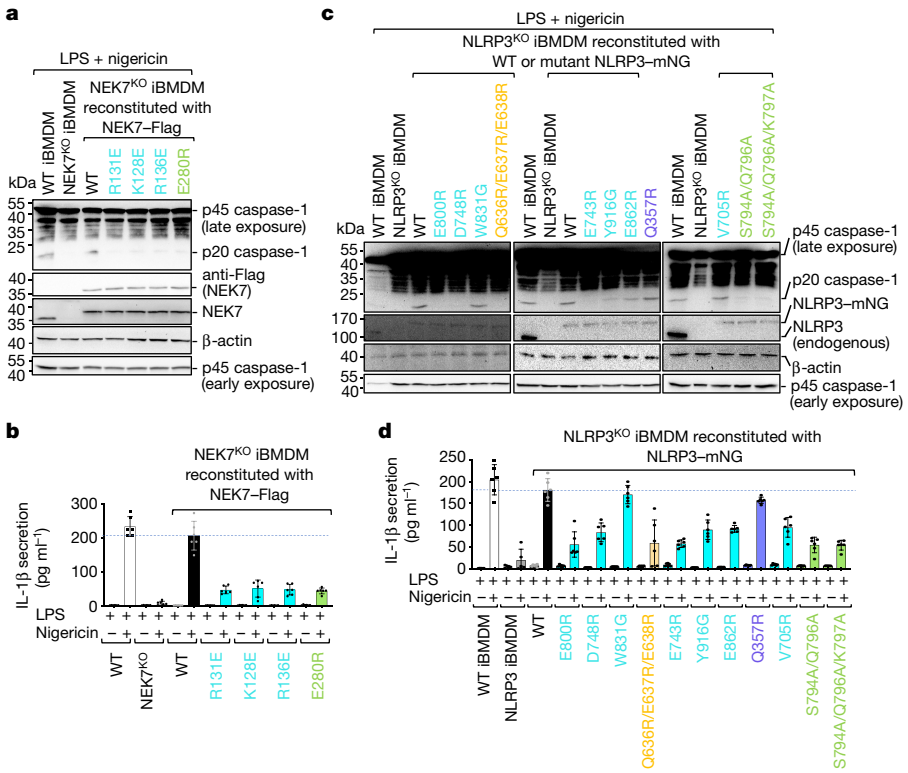

Fig. 4 | Structure-guided mutations of NLRP3 and NEK7 on inflammasome activation. NEK7 and NLRP3 mutations are coloured as in Fig. 3d, e, except that mutations on interactions *in trans* are coloured in green. **a**, **b**, NEK7-knockout (NEK7^{KO}) iBMDMs were reconstituted with wild-type or mutant Flag-tagged human NEK7, primed by LPS (4 h) and stimulated by nigericin (30 min). Cells were analysed by western blot for caspase-1 processing using a specific anti-caspase-1 antibody (repeated three times) (**a**). The full-length caspase-1 (p45) and processed large subunit of caspase-1 (p20) are labelled (first blot from the top). Caspase-1 p45 was also analysed by an early exposure to show equal loading (fifth blot). Reconstituted NEK7 was probed by anti-NEK7 and anti-Flag antibodies (second and third blots), and loading was analysed by an anti-β-actin antibody (fourth blot). Mature IL-1β released in the supernatant was measured by enzyme-linked immunosorbent assay (**b**). Data are presented as mean ± s.d. for $n = 3$ replicates each from 2 independent experiments. Dots, individual data points. **c**, **d**, NLRP3-knockout (NLRP3^{KO}) iBMDMs were reconstituted with wild-type or mutant human mNeonGreen (mNG)-tagged NLRP3, primed by LPS (4 h) and stimulated by nigericin (30 min). Caspase-1 processing (repeated 3 times) (**c**) and IL-1β release (shown as mean ± s.d. with $n = 3$ replicates each from 2 independent experiments) (**d**) were analysed as in **a**, **b**. Dots, individual data points. For gel source data, see Supplementary Fig. 1.

(Fig. 4c, Extended Data Fig. 7). The LRR mutants E800R, D748R and E743R were strongly defective in caspase-1 processing; it is possible that Y916G, E862R and V705R were partially defective. The LRR mutant W831A had no discernible effect. A triple mutation in the HD2 region (Q636R/E637R/E638R) was strongly defective. By contrast, the Q357R mutant in the NBD was not defective. Similarly, nigericin-induced IL-1β secretion and cell death showed a similar pattern of mutational effects (Fig. 4d, Extended Data Figs. 7, 8j), which supports the notion that the LRR and HD2 domains—but not the NBD—are imperative for the interaction between NLRP3 and NEK7.

The importance of the LRR may explain why a partial LRR construct of NLRP3 (amino acids 742–991) did not interact with NEK7[13], whereas a more-complete LRR domain construct (amino acids 711–1033) interacted with NEK7—albeit with some affinity reduction compared to the interaction with full-length NLRP3[14]. Consistently, NLRP3 phosphorylation at Y859 has a negative regulatory role[30]; Y859 is situated at the NEK7-binding site of LRR, the phosphorylation of which might cause steric hindrance and charge repulsion (Extended Data Fig. 8k). On the other hand, the tyrosine phosphatase PTPN22 (which dephosphorylates Y859) promotes NLRP3 activation; patients with inflammatory bowel disease who carry an autoimmunity-associated allele of *PTPN22* show increased IL-1β production[30]. Although the NACHT domain also contacts NEK7, the ability of NACHT alone to bind NEK7 remains unresolved. In one study, an LRR-deletion mutant (amino acids 1–741) did not interact with NEK7[13]. In another study, however, other LRR-deletion mutants (amino acids 1–686, 1–695, 1–710, 1–720 and 1–731) interacted with NEK7 and reconstituted *NLRP3*$^{-/-}$ macrophages for NLRP3 activation by multiple stimuli[31]. Constructs with shorter LRR truncations (amino acids 1–850, 1–879, 1–907, 1–936, 1–965 and 1–996) were inactive in reconstituting the activity of NLRP3[31].

Oligomeric assembly of the NLRP3–NEK7 complex

Previous studies on NLRC4 have shown that the NACHT domain undergoes a large rigid-body rotation at the HD1-to-WHD junction to open up the structure for oligomerization and activation[6,19,20,22,23]. We therefore modelled a hypothetical NLRP3 structure in an active conformation using the NLRC4 oligomer structure as a homology reference, which generates an approximately 90° rotation of the NBD–HD1 module (Fig. 5a). This modelling exercise placed the NBD–HD1–WHD module for direct interaction in the NLRP3 ring, without steric hindrance (Fig. 5b). By contrast, the inactive conformation is not compatible with the modelled oligomeric structure (Fig. 5c). The modelling should not affect NEK7 binding because only the NBD–HD1 module is moved relative to NEK7 (Extended Data Fig. 8l, Supplementary Video 2) and the NBD contact is not essential for NEK7 interaction, as shown by mutagenesis (Fig. 3d, e, 4c, d, Extended Data Fig. 8j).

Modelling of the hypothetical NLRP3–NEK7 inflammasome disc based on the NLRC4 oligomer places NEK7 at the oligomerization interface (Fig. 5b, d, Extended Data Fig. 9a). In particular, residue E280 of the NEK7 C-lobe (opposite from its NLRP3-interacting surface) contacts the neighbouring NLRP3 at residues S794, Q796 and K797, with a predicted buried surface area of 150 Å^2 (Fig. 5d). To test the functional importance of these predicted interactions in the modelled NLRP3 oligomer, we reconstituted NEK7-knockout or NLRP3-knockout iBMDMs using mutants on this new interface. As predicted, E280R or E280V did not affect the interaction between

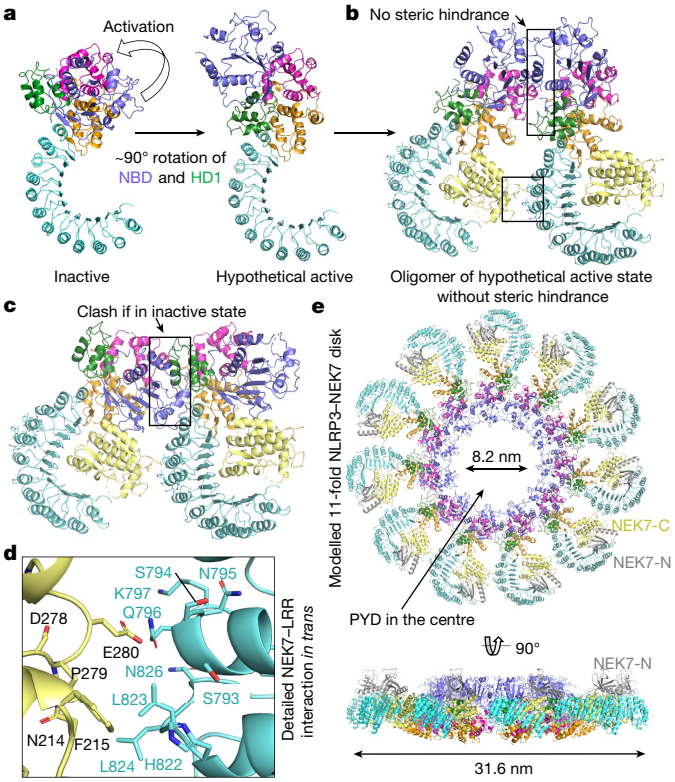

Fig. 5 | Modelling of active NLRP3 conformation and oligomerization. **a**, Modelled active NLRP3 (right) from its inactive structure (left) using the activation mechanism of NLRC4, in which the NBD–HD1 module rotates by 90° relative to the WHD–HD2–LRR module[19,20]. **b**, A dimer model of the active NLRP3–NEK7 complex based on the NLRC4 disk[20]. Interaction surfaces are boxed. **c**, A hypothetical inactive NLRP3 dimer would have created steric clashes at multiple sites in the NACHT domain. **d**, Magnified view showing the detailed NEK7–LRR interaction *in trans* boxed in **b**. Mutations at this interface compromised NLRP3 inflammasome activation as in Fig. 4. **e**, NLRP3–NEK7 inflammasome disk modelled after the NLRC4 11-subunit disk structure[20], shown in two orientations.

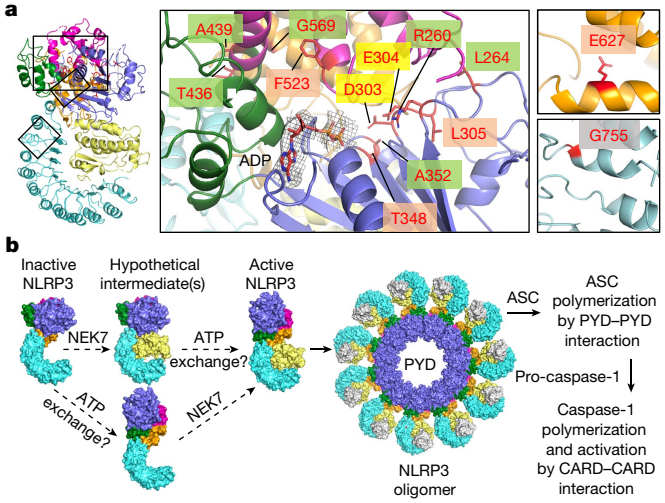

Fig. 6 | NLRP3 CAPS mutations and model of NEK7-mediated NLRP3 inflammasome activation. **a**, Structure mapping of all validated pathogenic mutations of NLRP3 from the Infevers website[33], highlighted by background colours behind residue labels. Density for ADP is shown (3σ). Green, disruption of inter-domain interactions in the inactive conformation; mauve, change of local conformation by mutating residues buried within the domains; yellow, alteration in key residues in the Walker B motif; grey, enhancement of NEK7 binding. **b**, A proposed two-step NLRP3 inflammasome activation model. CARD, caspase recruitment domain.

NEK7 and NLRP3 in a pulldown assay using recombinant proteins, as E280 resides on the side of NEK7 opposite its NLRP3-binding site (Fig. 3d, e). However, NEK7(E280R) did not rescue NLRP3 activation in NEK7-knockout iBMDMs, whereas wild-type NEK7 did (Fig. 4a, b, Extended Data Fig. 8f). The double mutant NLRP3(S794A/Q796A) and the triple mutant NLRP3(S794A/Q796A/K797A) both failed to reconstitute NLRP3-induced caspase-1 processing, IL-1β secretion and cell death in NLRP3-knockout iBMDMs, whereas wild-type NLRP3 did (Fig. 4c, d, Extended Data Fig. 8j). To confirm that NLRP3 inflammasome assembly per se was disrupted by these mutations, we assessed NLRP3 inflammasome speck formation using immunofluorescence imaging. Whereas wild-type NEK7 and NLRP3 rescued speck formation in NEK7-knockout or NLRP3-knockout iBMDMs, the NEK7 and NLRP3 mutants all failed to form speck in reconstituted iBMDMs upon nigericin stimulation (Extended Data Fig. 9b).

The NLRC4 inflammasome also has an additional oligomerization interface at the LRR (Extended Data Fig. 9c). Moreover, the recently identified NLRC4 autoinflammatory mutation W655C at this LRR–LRR interface (Extended Data Fig. 9d) promotes NLRC4 inflammasome assembly, probably by enhancing the LRR–LRR interaction, and causes macrophage activation syndrome in human[32]. In NLRP3, the LRR itself is too short to reach the adjacent LRR in the hypothetical oligomer, and NEK7 bridges the gap between adjacent NLRP3 subunits. Collectively, these data support our model of NLRP3 activation and point to a previously unanticipated mechanism for NEK7 requirement. In the modelled complex with full-length NEK7, the NEK7 N-lobe projects away from the plane of the inflammasome ring and does not interfere with NLRP3 oligomerization (Fig. 5e).

NLRP3 CAPS mutations

To investigate the mechanism of autoinflammation in CAPS, we mapped the validated pathogenic mutations of NLRP3 from the Infevers website[33] to the structure (Fig. 6a, Extended Data Fig. 9e). These mutations are associated with Muckle–Wells syndrome, neonatal onset multisystem inflammatory disease and familial cold autoinflammatory syndrome. Notably, almost all the mutations lie in the NACHT domain and surround the ADP-binding site. One exception is G755 in the LRR near the NEK7-binding site, which exhibited enhanced interaction with NEK7 when mutated to alanine or arginine[14].

Structural analysis suggests that the NACHT mutations may affect the inactive conformation, and therefore enhance NLRP3 activation. These mutations may be categorized into three tiers: (1) those that reside at the inter-domain interfaces, and thus affect the important interactions that stabilize the inactive conformation (R260, L264, D303, A352, T436, A439 and G569); (2) those that are on the Walker B motif of the ATPase (D303, which coordinates Mg^{2+} ions; and E304 for ATP hydrolysis[34]); and (3) those that are buried within their respective domains (L305, T348, F523 and E627), in which mutations may affect the local domain conformation and indirectly destabilize the inter-domain interactions in the inactive state. Whereas L305, T348 and F523 are uncharged, E627 forms a partially buried salt-bridge with R548 and K568 in the NLRP3 structure.

Conclusion

In summary, our structural and functional studies have demonstrated that the NLRP3–NEK7 interaction dictates the NEK7 requirement for NLRP3 inflammasome activation. We further show that the opposite side of NEK7—which is not required for the initial NLRP3 interaction—is important for stimulus-dependent NLRP3 activation, by bridging oligomerization. We propose that NLRP3 activation requires at least two steps (Fig. 6b). First, NLRP3 needs to be bound to NEK7, a process that is enhanced by priming and NLRP3 triggers[13,14]. Second, the formation of the NLRP3–NEK7 complex alone may not be sufficient to induce NLRP3 activation, because NLRP3 oligomer-

ization also requires the conversion of NACHT from an inactive to an active conformation. This conformational transition may require ATP binding and other unknown allosteric triggers, as NLRP3 has previously been shown to possess ATPase activity[34]. In the NACHT-domain-containing protein APAF-1, binding of ATP or an ATP analogue—but not ATP hydrolysis—is required for APAF-1 activation[35]. The necessities of both NEK7 binding and the NACHT conformational change for NLRP3 activation are supported by the NEK7 requirement in mouse macrophages that contain the CAPS-associated activating mutant NLRP3(R258W) (equivalent to human NLRP3(R260W)) (Fig. 6a, Extended Data Fig. 9e) for the activation of caspase-1[13]. NLRP3 activation is complicated by many factors, including post-translational modifications[36–39], but our studies may have unravelled the mechanism for the NEK7-licensed NLRP3 inflammasome activation.

Our in vitro-reconstituted NLRP3–NEK7 complex is clearly in an inactive state and we did not observe oligomers of the purified NLRP3–NEK7 heterodimer. ATP or ATP analogues, which can induce conformational changes and oligomerization of APAF-1, did not induce oligomerization of the NLRP3–NEK7 heterodimer in vitro. We reasoned that this may be because NEK7 binding licenses NLRP3 but is insufficient for inflammasome assembly. Despite extensive studies, the direct triggers for the NLRP3 conformational change required to mediate the inflammasome assembly are unknown. In this regard, it is unclear whether one activated NLRP3–NEK7 complex will trigger a nucleated oligomerization, similar to the PrgJ–NAIP2–NLRC4 inflammasome[6,19,20], or whether the direct activator has to induce the conformational change of each NLRP3 molecule for inflammasome assembly. In plants, NLR-mediated effector-triggered immunity is often indirect, in that multiple microbial effectors may first modify a common NLR-associated protein or a specific domain in an NLR, which then relays the invasion signal to the NLR for effector-triggered immunity[40]. For NLRP3, it remains to be addressed whether NEK7 can be considered a common sensor of this type.

Online content

Any methods, additional references, Nature Research reporting summaries, source data, extended data, supplementary information, acknowledgements, peer review information; details of author contributions and competing interests; and statements of data and code availability are available at https://doi.org/10.1038/s41586-019-1295-z.

Received: 21 January 2019; Accepted: 16 May 2019;
Published online 12 June 2019.

1. Lamkanfi, M. & Dixit, V. M. Mechanisms and functions of inflammasomes. *Cell* **157**, 1013–1022 (2014).
2. Broz, P. & Dixit, V. M. Inflammasomes: mechanism of assembly, regulation and signalling. *Nat. Rev. Immunol.* **16**, 407–420 (2016).
3. Guo, H., Callaway, J. B. & Ting, J. P. Inflammasomes: mechanism of action, role in disease, and therapeutics. *Nat. Med.* **21**, 677–687 (2015).
4. Shi, J., Gao, W. & Shao, F. Pyroptosis: gasdermin-mediated programmed necrotic cell death. *Trends Biochem. Sci.* **42**, 245–254 (2017).
5. Liu, X. et al. Inflammasome-activated gasdermin D causes pyroptosis by forming membrane pores. *Nature* **535**, 153–158 (2016).
6. Hu, Z. et al. Crystal structure of NLRC4 reveals its autoinhibition mechanism. *Science* **341**, 172–175 (2013).
7. Lu, A. et al. Unified polymerization mechanism for the assembly of ASC-dependent inflammasomes. *Cell* **156**, 1193–1206 (2014).
8. Lu, A. et al. Molecular basis of caspase-1 polymerization and its inhibition by a new capping mechanism. *Nat. Struct. Mol. Biol.* **23**, 416–425 (2016).
9. Lu, A. et al. Plasticity in PYD assembly revealed by cryo-EM structure of the PYD filament of AIM2. *Cell Discov.* **1**, 15013 (2015).
10. Rathinam, V. A., Vanaja, S. K. & Fitzgerald, K. A. Regulation of inflammasome signaling. *Nat. Immunol.* **13**, 333–342 (2012).
11. Muñoz-Planillo, R. et al. K^+ efflux is the common trigger of NLRP3 inflammasome activation by bacterial toxins and particulate matter. *Immunity* **38**, 1142–1153 (2013).
12. Chen, J. & Chen, Z. J. PtdIns4P on dispersed *trans*-Golgi network mediates NLRP3 inflammasome activation. *Nature* **564**, 71–76 (2018).
13. He, Y., Zeng, M. Y., Yang, D., Motro, B. & Núñez, G. NEK7 is an essential mediator of NLRP3 activation downstream of potassium efflux. *Nature* **530**, 354–357 (2016).
14. Shi, H. et al. NLRP3 activation and mitosis are mutually exclusive events coordinated by NEK7, a new inflammasome component. *Nat. Immunol.* **17**, 250–258 (2016).
15. Schmid-Burgk, J. L. et al. A genome-wide CRISPR (clustered regularly interspaced short palindromic repeats) screen identifies NEK7 as an essential component of NLRP3 inflammasome activation. *J. Biol. Chem.* **291**, 103–109 (2016).
16. Shi, H., Murray, A. & Beutler, B. Reconstruction of the mouse inflammasome system in HEK293T cells. *Bio Protoc.* **6**, e1986 (2016).
17. Coll, R. C. et al. A small-molecule inhibitor of the NLRP3 inflammasome for the treatment of inflammatory diseases. *Nat. Med.* **21**, 248–255 (2015).
18. Dar, A. C., Dever, T. E. & Sicheri, F. Higher-order substrate recognition of eIF2α by the RNA-dependent protein kinase PKR. *Cell* **122**, 887–900 (2005).
19. Hu, Z. et al. Structural and biochemical basis for induced self-propagation of NLRC4. *Science* **350**, 399–404 (2015).
20. Zhang, L. et al. Cryo-EM structure of the activated NAIP2-NLRC4 inflammasome reveals nucleated polymerization. *Science* **350**, 404–409 (2015).
21. Maekawa, S., Ohto, U., Shibata, T., Miyake, K. & Shimizu, T. Crystal structure of NOD2 and its implications in human disease. *Nat. Commun.* **7**, 11813 (2016).
22. Yang, X. et al. Structural basis for specific flagellin recognition by the NLR protein NAIP5. *Cell Res.* **28**, 35–47 (2018).
23. Tenthorey, J. L. et al. The structural basis of flagellin detection by NAIP5: a strategy to limit pathogen immune evasion. *Science* **358**, 888–893 (2017).
24. Kelley, L. A., Mezulis, S., Yates, C. M., Wass, M. N. & Sternberg, M. J. The Phyre2 web portal for protein modeling, prediction and analysis. *Nat. Protoc.* **10**, 845–858 (2015).
25. Richards, M. W. et al. An autoinhibitory tyrosine motif in the cell-cycle-regulated Nek7 kinase is released through binding of Nek9. *Mol. Cell* **36**, 560–570 (2009).
26. Qu, Y. et al. Phosphorylation of NLRC4 is critical for inflammasome activation. *Nature* **490**, 539–542 (2012).
27. Suzuki, S. et al. *Shigella* type III secretion protein MxiI is recognized by Naip2 to induce Nlrc4 inflammasome activation independently of Pkcδ. *PLoS Pathog.* **10**, e1003926 (2014).
28. Krissinel, E. & Henrick, K. Inference of macromolecular assemblies from crystalline state. *J. Mol. Biol.* **372**, 774–797 (2007).
29. Haq, T. et al. Mechanistic basis of Nek7 activation through Nek9 binding and induced dimerization. *Nat. Commun.* **6**, 8771 (2015).
30. Spalinger, M. R. et al. NLRP3 tyrosine phosphorylation is controlled by protein tyrosine phosphatase PTPN22. *J. Clin. Invest.* **126**, 1783–1800 (2016).
31. Hafner-Bratković, I. et al. NLRP3 lacking the leucine-rich repeat domain can be fully activated via the canonical inflammasome pathway. *Nat. Commun.* **9**, 5182 (2018).
32. Moghaddas, F. et al. Autoinflammatory mutation in NLRC4 reveals a leucine-rich repeat (LRR)-LRR oligomerization interface. *J. Allergy Clin. Immunol.* **142**, 1956–1967.e6 (2018).
33. Touitou, I. et al. Infevers: an evolving mutation database for auto-inflammatory syndromes. *Hum. Mutat.* **24**, 194–198 (2004).
34. Duncan, J. A. et al. Cryopyrin/NALP3 binds ATP/dATP, is an ATPase, and requires ATP binding to mediate inflammatory signaling. *Proc. Natl Acad. Sci. USA* **104**, 8041–8046 (2007).
35. Jiang, X. & Wang, X. Cytochrome *c* promotes caspase-9 activation by inducing nucleotide binding to Apaf-1. *J. Biol. Chem.* **275**, 31199–31203 (2000).
36. Song, N. & Li, T. Regulation of NLRP3 inflammasome by phosphorylation. *Front. Immunol.* **9**, 2305 (2018).
37. Barry, R. et al. SUMO-mediated regulation of NLRP3 modulates inflammasome activity. *Nat. Commun.* **9**, 3001 (2018).
38. Py, B. F., Kim, M. S., Vakifahmetoglu-Norberg, H. & Yuan, J. Deubiquitination of NLRP3 by BRCC3 critically regulates inflammasome activity. *Mol. Cell* **49**, 331–338 (2013).
39. Mangan, M. S. J. et al. Targeting the NLRP3 inflammasome in inflammatory diseases. *Nat. Rev. Drug Discov.* **17**, 688 (2018).
40. Khan, M., Subramaniam, R. & Desveaux, D. Of guards, decoys, baits and traps: pathogen perception in plants by type III effector sensors. *Curr. Opin. Microbiol.* **29**, 49–55 (2016).
41. Kucukelbir, A., Sigworth, F. J. & Tagare, H. D. Quantifying the local resolution of cryo-EM density maps. *Nat. Methods* **11**, 63–65 (2014).

METHODS

Cloning, expression, purification and reconstitution of recombinant human NLRP3 and NEK7 complex. Full-length (amino acids 1–302) and N-terminally truncated (amino acids 31–302) human NEK7 sequences were cloned into a modified pET28a vector with an N-terminal 6×His-SUMO tag followed by the Ulp1 protease site. These constructs were transfected into *Escherichia coli* BL21 (DE3) cells, which were grown in LB medium supplemented with 50 μg/ml kanamycin. Protein expression was induced overnight at 18 °C with 0.2 mM isopropyl-β-D-thiogalactopyranoside after optical density at 600 nm reached 0.8. For N-terminally truncated NEK7, cells were collected and resuspended in a lysis buffer containing 20 mM Tris-HCl at pH 7.4, 300 mM NaCl, 0.5 mM Tris(2-carboxyethyl) phosphine hydrochloride (TCEP) and 20 mM imidazole. For the full-length NEK7, the lysis was performed in buffer containing 50 mM Tris-HCl at pH 7.5, 500 mM NaCl, 5 mM $MgCl_2$, 10 mM imidazole, 10% glycerol and 2 mM β-mercaptoethanol. The proteins were first purified by affinity chromatography using Ni-NTA beads (Qiagen). The 6×His–SUMO tag was cleaved by overnight Ulp1 protease digestion with dialysis at 4 °C and removed by passing through Ni-NTA beads again. The NEK7 proteins with SUMO-tag or after protease cleavage were further purified by size-exclusion chromatography on a Superdex 200 column (GE Healthcare Life Sciences) equilibrated with the gel filtration buffer containing 20 mM Tris-HCl at pH 7.5, 150 mM NaCl and 0.5 mM TCEP.

An artificial NEK7 dimer was engineered based on the protein kinase R dimer structure (PDB code 2A19)[18] by a back-to-back interaction at the N-terminal lobe. The N-terminal disordered region (residues 1–33) of NEK7 was replaced by the non-canonical helix α0 (residues 258–266) of protein kinase R, and several surface residues at the predicted dimerization interface were mutated to corresponding residues in protein kinase R (L54R, V58K, P59T, K87A, A99V, S100C, E103T and D104G). Protein expression and purification of the NEK7 dimer followed the same procedure as full-length or N-terminally truncated wild-type NEK7.

NLRP3 with the pyrin domain deleted (amino acids 134–1034) was cloned into a modified pFastBac vector with an N-terminal MBP tag. The sequence 134-YRKKYRK-140 was changed to 134-YCAKYRA-140, designed to avoid a potential clash with the N-terminal MBP. The baculovirus of NLRP3 was prepared using the Bac-to-Bac system (Invitrogen). To express the protein, 10 ml of the NLRP3 baculovirus was used to infect 1 l Sf9 cells, which were collected 48 h after infection. Cells were lysed by sonication in buffer containing 20 mM Tris-HCl at pH 7.5, 200 mM NaCl, 0.5 mM TCEP and 10% glycerol with freshly added protease inhibitor cocktail (Sigma). After centrifugation, the supernatant was incubated with 3 ml amylose resin at 4 °C for 1 h. The mixture was then subjected to gravity flow and the bound MBP-tagged NLRP3 protein was eluted with 25 mM maltose. The eluted protein was further purified by size-exclusion chromatography on a Superose 6 column (GE Healthcare Life Sciences) in the same gel filtration buffer used for NEK7.

The complexes of MBP-tagged NLRP3 with NEK7 monomer and dimer were reconstituted by size-exclusion chromatography on a Superose 6 column equilibrated with the gel filtration buffer. The eluted proteins were analysed on SDS–PAGE gels for homogeneity and stoichiometry. The fractions were then pooled and concentrated for further analysis and cryo-EM data collection.

All mutagenesis experiments were performed by the QuikChange site-directed mutagenesis protocol using Q5 High-Fidelity 2× Master Mix (NEB). All plasmids were verified by DNA sequencing.

Microscale thermophoresis. Proteins were labelled with the cysteine-reactive dye Alexa Fluor 488 C5 maleimide (Thermo Fisher). Purified NLPR3 was incubated with ~20-fold molar excess of the dye in gel-filtration buffer for 1 h. After labelling, the excess dye was removed by applying the sample on Superdex 200 column equilibrated with the gel filtration buffer. Tween 20 (0.05%) was added to the protein buffer for microscale thermophoresis measurements before the experiment.

Datasets were collected at a temperature of 25.1 °C. For the Alexa Fluor 488-labelled NLRP3 interaction with NEK7, a concentration series of NEK7 was prepared using a 1:1 serial dilution of NEK7 in gel filtration buffer supplemented with 0.05% Tween 20. The range of NEK7 concentration used was from 32.5 μM to a final concentration of 1 nM, over 16 serial diluted capillaries with 10-μl samples. The interaction was initiated by the addition 10 μl of 140 nM Alexa Fluor 488-labelled NLRP3 to each reaction mixture, resulting in a 70 nM final concentration of NLRP3. The LED power was 100% and the microscale thermophoresis power (that is, the power supplied to the infrared laser) was 60%. The pre-microscale thermophoresis period was 5 s, the microscale thermophoresis acquisition period was 20 s, and the post- microscale thermophoresis period was 5 s. Data were analysed by MO Control software provided by NanoTemper. For analysis, the 32.5 μM concentration measurement was deleted as an outlier.

Multi-angle light scattering. For molecular-mass determination by multi-angle light scattering (MALS), protein samples were injected into a Superdex 200 (10/300 GL) gel-filtration column equilibrated with the gel filtration buffer. The chromatography system was attached to a three-angle light scattering detector (miniDAWN TRISTAR) and a refractive index detector (Optilab DSP) (Wyatt Technology). Data were collected every 0.5 s with a flow rate of 0.5 ml/min. Data analysis was carried out using ASTRA V.

Negative-staining electron microscopy. For negative staining, 4 μl of an NLRP3–NEK7 complex was placed onto a glow-discharged copper grid (Electron Microscopy Sciences) coated with a layer of thin carbon, washed twice with H_2O, stained with 1–2% uranyl formate for 30 s and air-dried. The grids were imaged on a Tecnai G2 Spirit BioTWIN electron microscope and recorded with an AMT 2k CCD camera (Harvard Medical School Electron Microscopy Facility).

Cryo-EM data collection. An NLRP3–NEK7 complex at 0.7 mg/ml was incubated with 0.3 mM ADP, 5 mM $MgCl_2$ and 0.3 mM MCC950 on ice for 30 min. A 3-μl drop of the NLRP3–NEK7 complex was applied to a glow-discharged Quantifoil grid (R 1.2/1.3 400 mesh, copper, Electron Microscopy Sciences), blotted for 3–3.5 s in 100% humidity at 4 °C and plunged into liquid ethane using an FEI Vitrobot Mark IV. For data collection on an FEI Talos Arctica microscope operating at an acceleration voltage of 200 keV, movies were acquired on a K2 Summit direct electron detector (Gatan) in super-resolution counting mode, with 10.03 s total exposure time over 59 frames and an accumulated dose of 58.1 electrons per $Å^2$. The super-resolution pixel size was 0.5843 Å. The defocus level in the data collection was set in the range of −1.0 to −3.0 μm. A total of 3,667 movies were collected.

For data collection on an FEI Titan Krios G2 microscope operating at 300 keV, the cryo-grids were visually inspected for ice contaminations and flatness before loading into the microscope autoloader. Data collection used post-column BioQuantum energy filter (Gatan) in zero-loss imaging mode with a 20-μm energy slit and K2 Summit direct electron detector (Gatan) in super-resolution counting mode (Peking University Electron Microscopy Laboratory and Cryo-EM Platform). Although the grids appeared to have icy areas, there were plenty of good holes, which yielded images that were free of strong diffraction patterns corresponding to crystalline ice. Coma-free alignment was manually optimized before data collection; the parallel-beam illumination area under a nanoprobe mode was selected to achieve the optimal dose rate, avoid exposure interference and minimize edge fringes on the image. To increase collection efficiency, the data were collected in part with multiple exposures per grid hole, during which the image shift applied was no more than 250 nm. The data collection process was set up and carried out in SerialEM[42]. Movies were acquired with a dose rate of 5.4 electrons per second per physical pixel, and a total dose of 54.8 electrons per $Å^2$ equally distributed in 7.2 s to 40 frames. The super-resolution pixel size was 0.42 Å. A total of 15,861 movies were collected during 5 separate sessions, among which 1,340 movies were collected with a moderate stage tilt of 20°. The defocus levels of the images were set in the range of −0.8 to −3.0 μm.

Cryo-EM data processing. For Arctica data processing, raw movies were corrected by gain reference and for beam-induced motion, and summed into motion-corrected images using MotionCor2[43]. The CTFFIND4 program[44] was used to determine the actual defocus level of each micrograph. RELION 3.0[45] and cisTEM[46] were used for subsequent image processing (Extended Data Fig. 2). First, template-free autopicking was used to generate an initial particle set for 2D classification. Good 2D classes were then used as templates for additional autopicking. Almost one million particles were picked which were subjected to multiple rounds of 2D classification until the classes looked homogenous. A few good class averages in different orientations were selected for the reconstruction of an initial model, which was low-pass-filtered to 60.0 Å to use as the input reference for 3D classification of 522,320 particles. One selected 3D class was further classified and refined to reach an overall resolution of 4.3 Å, measured by gold-standard Fourier shell correlation (FSC) between half maps (Extended Data Table 1). Owing to particle orientation preference, the map suffers from anisotropic resolution.

Krios data processing also used MotionCor2[43] for aligning and summing movie frames at the pixel size 0.84 Å. The averaged images were binned threefold to obtain TIFF images for visual screening. Bad images, such as those with excessive ice contaminants, were removed. The contrast-transfer function parameters of each drift-corrected micrograph were then calculated using the program Gctf[47]. Particles were automatically picked from twofold-binned micrographs using Gautomatch (https://sbgrid.org/software/titles/gautomatch) and a Gaussian sphere template, which yielded a total of 1,850,332 particles. Reference-free 2D and 3D classifications were carried out with both RELION 3.0[45] and ROME 1.1.2[48]. The latter combines maximum-likelihood-based image alignment with statistical machine-learning-based classification[48], and can output a large number of refined 2D classes with subtle differences. The NLRP3–NEK7 complex particles naturally and preferentially orientated with the curved LRR plane on the grid plane. To alleviate this orientation preference, we first included a subset of data that was collected with a modest 20° stage tilt. Because of the large vertical drift of carbon grids projected in the lateral direction, we could not use a larger tilt. We also retained as many particles as possible from the rare views that may not have been previously included in RELION-based 2D classification. This was done by multiple

rounds of deep unsupervised 2D classifications with the ROME 1.1.2 package[48], which allowed us to improve the conformational homogeneity of selected particles. Three-dimensional classification and refinement were carried out in Relion 3.0[45]. Map reconstruction was done with ROME 1.1.2[48], and the local resolution map was produced with ResMap[41], which is embedded in RELION 3.0[45] (Extended Data Fig. 3). The inclusion of the tilted data and deep 2D classification spread out the orientation distribution and helped to improve the overall features, such as the connecting loop density on both sides of the LRR region. Data processing statistics are summarized in Extended Data Table 1.

Model building and display. NLRP3 initial homology model was generated using the Phyre2 server[24]. Manual adjustment, rigid-body fitting, flexible fitting and segment-based real-space refinement were performed in distinct parts of the initial model to fit in the density in Coot[49], with help of Chimera[50] and real-space refinement in Phenix[51]. In the fitting to the final 3.8 Å map, large side-chain densities were used to guide the local register of the backbone trace. For example, W774 and W831 flanking the inner surface of the LRR domain were used to confirm the residue register in LRR. The density that we observed accounts for NLRP3 residues (amino acids 133–1034) that include the NBD, HD1, WHD, HD2 and LRR domains. A few unstructured regions, including part of the HD2 domain (amino acids 654–683), were omitted owing to poor density. The model was fitted and modelled to the best of our knowledge. The remaining part of the cryo-EM map was fitted with the NEK7 crystal structure (PDB code 2WQN)[25]. Only NEK7 C-terminal lobe residues (amino acids 113–300) were fitted in the density because the N-lobe density appeared to have been averaged out in the data processing, probably owing to flexibility. Interaction analysis was conducted using PISA[28] and structure representations were generated in Chimera[50], Pymol[52] and ResMap[41].

Thermal shift assay. Purified 2 μM NLRP3 or NEK7 was mixed with 1-fold protein thermal shift dye (Thermo fisher scientific) and 200 μM MCC950 or ADP, or 100 μM MCC950 plus 100 μM ADP in a 20-μl reaction volume. Thermal scanning (25 to 75 °C at 1.5 °C per minute) was performed, and melting curves were recorded on a StepOne RT–PCR machine. Data analysis was done by Protein Thermal Shift software (Thermo Fisher Scientific).

In vitro pull-downs. MBP-tagged NLRP3 (1.5 μM) was mixed with 3 μM full-length wild-type or mutant NEK7 in buffer containing 30 mM HEPES at pH 7.5, 150 mM NaCl and 0.5 mM TCEP, and incubated for 1 h on ice. The mixture was further incubated for 1 h with 30 μl amylose resin and washed twice with 250 μl of the same buffer, followed by 1 h elution with 50 mM maltose. Input and elution fractions were analysed with SDS–PAGE. NEK7 and NLRP3 bands were quantified with ImageJ and the efficiency of binding was calculated from the ratio of NEK7 to NLRP3 band intensities. Three independent experiments were performed, and the efficiency of binding was presented as mean ± standard deviation.

Generation of stable cell lines and cellular reconstitution. To reconstitute NLRP3-knockout iBMDMs with wild-type or mutant full-length mNG-tagged human NLRP3, lentiviral particles were generated as follows. On day 0, the lentivirus was produced using HEK293T (60% confluent) cells by co-transfecting 1 μg of a pLV vector containing the wild-type or mutant NLRP3, 750 ng psPAX2 packaging plasmid and 250 ng pMD2.G envelope plasmid. The packaging and envelope plasmids were gifts from D. Trono (Addgene numbers 12260 and 12259, respectively). The transfected cells were incubated overnight. On day 1, the medium was removed, and replenished with 1 ml fresh medium. The cells were incubated for another day. The expression was analysed by a confocal laser scanning microscope FluoView FV1000 (Olympus America), equipped with 488 argon for green excitation.

On day 2, the supernatant containing the virus was filtered using a 0.45-μm filter and used directly to infect NLRP3-knockout iBMDMs (2.5×10^6 cells/ml) using a spinfection protocol to increase the efficacy. Spinfection was performed at 2,500*g* for 90 min at 37 °C using 8 μg/ml polybrene (Santa Cruz Biotechnology, cat. no. sc-134220). After spinfection, cells were further incubated for the expression of reconstituted proteins for 48 h. Reconstitution was verified by western blotting using a specific anti-human NLRP3 antibody (Adipogen, cat no. AG-20B-0014-C100).

Inflammasome activation assays. NLRP3-knockout iBMDMs reconstituted with human wild-type or mutant NLRP3 were seeded at a density of 3×10^6 cells/ml. On the next day, the cells were primed with 1 μg/ml LPS (Invivogen, cat. no. tlrl-b5lps) for 4 h. Post priming, the cells were activated with 20 μM nigericin (Sigma-Aldrich, cat. no. N7143-5MG) for 30 min, and the supernatant was collected. Released IL-1β was analysed using an ELISA kit (Affymetrix eBioscience, cat. no. 88-7013), and released LDH was measured using the LDH Glo cytotoxicity assay (Promega, cat. no. J2380), according to manufacturer's instructions. For analysis of caspase-1 cleavage, the whole-cell lysate was prepared in 1× laemmli sample buffer, resolved on 12.5% SDS–PAGE and western-blotted using a specific anti-mouse caspase-1 antibody (Adipogen, cat. no. AG-20B-0042-C100). The graphs were plotted using GraphPad Prism 7 software.

Immunolabelling and antibodies. Reconstituted iBMDM cells were primed for 4 h with LPS, and then activated with nigericin for 30 min. Fixative, permeabilization and blocking buffers were prepared in Brinkley Buffer 80 (BRB80), and kept at 37 °C before use. BRB80 buffer was prepared freshly using 80 mM PIPES, 1 mM $MgCl_2$, 1 mM EGTA, titrated to pH 6.8 with a saturated solution of KOH.

Cells were fixed in 3.7% paraformaldehyde for 5 min at room temperature. Afterwards, cells were washed twice using BRB80 with 5-min intervals between washes. Permeabilization was carried out for 5 min at room temperature using 0.15% Triton X-100 (in 1× BRB80). Washing was carried out to remove permeabilization buffer. Cells were then blocked for 1 h at room temperature using blocking buffer (3% gelatin from cold water fish skin prepared in 1× BRB80). Cells were incubated with primary antibody for overnight (anti-ASC, 1:1,000, Cell Signaling Technology, cat. no. 67824S). The cells were washed and incubated with secondary antibody for an hour at room temperature (Goat anti-rabbit (H+L), Alexa Fluor 647 HRP conjugated 1:1,000 Thermo Fisher Scientific, cat. no. A- 21245). The nucleus was stained using Hoechst 33342 (Invitrogen, cat. no. H3750). In between each step, extensive washing steps were carried out to remove unbound antibodies and stains.

Confocal laser-scanning microscopy. After activation, reconstituted iBMDMs were washed once with 1× BRB buffer, fixed and labelled with antibodies as mentioned in 'Immunolabelling and antibodies'. Confocal sections were obtained with an Olympus confocal laser scanning microscope FluoView FV1000 (Olympus America), equipped with 405 diode (for blue excitation) or a 635 diode (for far-red excitation). Images were captured using 40× (0.95 NA, air objective), with Olympus FluoView version 3.0 viewer software. The images were acquired identically, and processed using Adobe Photoshop software.

Reporting summary. Further information on research design is available in the Nature Research Reporting Summary linked to this paper.

Data availability

The cryo-EM map has been deposited in the Electron Microscopy Data Bank under the accession number EMD-0476. The atomic coordinates have been deposited in the Protein Data Bank under the accession number 6NPY. All other data can be obtained from the corresponding author upon reasonable request.

42. Mastronarde, D. N. Automated electron microscope tomography using robust prediction of specimen movements. *J. Struct. Biol.* **152**, 36–51 (2005).
43. Zheng, S. Q. et al. MotionCor2: anisotropic correction of beam-induced motion for improved cryo-electron microscopy. *Nat. Methods* **14**, 331–332 (2017).
44. Rohou, A. & Grigorieff, N. CTFFIND4: Fast and accurate defocus estimation from electron micrographs. *J. Struct. Biol.* **192**, 216–221 (2015).
45. Zivanov, J. et al. New tools for automated high-resolution cryo-EM structure determination in RELION-3. *eLife* **7**, e42166 (2018).
46. Grant, T., Rohou, A. & Grigorieff, N. *cis*TEM, user-friendly software for single-particle image processing. *eLife* **7**, e35383 (2018).
47. Zhang, K. Gctf: real-time CTF determination and correction. *J. Struct. Biol.* **193**, 1–12 (2016).
48. Wu, J. et al. Massively parallel unsupervised single-particle cryo-EM data clustering via statistical manifold learning. *PLoS ONE* **12**, e0182130 (2017).
49. Emsley, P., Lohkamp, B., Scott, W. G. & Cowtan, K. Features and development of Coot. *Acta Crystallogr. D* **66**, 486–501 (2010).
50. Pettersen, E. F. et al. UCSF Chimera—a visualization system for exploratory research and analysis. *J. Comput. Chem.* **25**, 1605–1612 (2004).
51. Adams, P. D. et al. PHENIX: a comprehensive Python-based system for macromolecular structure solution. *Acta Crystallogr. D* **66**, 213–221 (2010).
52. Delano, W. L. The PyMol Molecular Graphics System https://pymol.org/2/ (2002).
53. Scheres, S. H. RELION: implementation of a Bayesian approach to cryo-EM structure determination. *J. Struct. Biol.* **180**, 519–530 (2012).
54. Robert, X. & Gouet, P. Deciphering key features in protein structures with the new ENDscript server. *Nucleic Acids Res.* **42**, W320–W320 (2014).

Acknowledgements We thank the University of Massachusetts Cryo-EM Core Facility and the National Cryo-EM Facility at the National Cancer Institute for 200-keV data collection, the Electron Microscopy Laboratory and Cryo-EM Platform at Peking University for 300-keV data collection, and C. Xu, K. Song, K. Lee, X. Li, Y. Ma and D. Yu for technical support. This work was funded in part by the US NIH grant DP1HD087988 (H.W.), R01AI124491 (H.W.), R01AI06331 (G.N.), an Intel Corporation academic grant (Y.M.), the Thousand Talents Plan of China (Y.M.), National Natural Science Foundation of China grant 11774012 (Y.M.) and Natural Science Foundation of Beijing City grant Z180016 (Y.M.). Data processing was performed in part in the Sullivan cluster, which is funded in part by a gift from Mr. and Mrs. D. J. Sullivan Jr, and in the Weiming No.1 and Life Science No. 1 High-Performance Computing Platform at Peking University. We thank H. Leung (PCMM, BCH confocal core facility manager).

Author contributions H.W., L.W. and H.S. conceived the study. L.W. designed constructs. L.W., Q.Q. and H.S. purified the complexes, and H.S., L.W. and Q.Q. made cryo-grids for data collection. H.S., L.W., W.L.W., Q.Q., Z.W. and Y.M. collected data. H.S., W.L.W. and Q.Q. analysed cryo-EM data, and H.W. and Y.M. supervised data processing. H.S. performed initial model

building and refinement, and W.L.W. and Y.M. performed additional model fitting and refinement. H.S. designed mutants for in vitro and cell-based assays. V.G.M. performed all cell-based assays. L.A. and A.V.H. performed NEK7-mutant assays. G.N. provided reagents for cell-based assays and valuable discussions. H.W., H.S. and Y.M. wrote the manuscript, and all authors provided comments on the manuscript.

Competing interests L.W. and A.V.H. are employees, and H.W. is co-founder, of SMOC Therapeutics; the other authors declare no competing interests.

Additional information

Supplementary information is available for this paper at https://doi.org/10.1038/s41586-019-1295-z.

Correspondence and requests for materials should be addressed to Y.M. or H.W.

Peer Reviewer information: *Nature* thanks Eicke Latz, Edward Miao and the other anonymous reviewer(s) for their contribution to the peer review of this work.

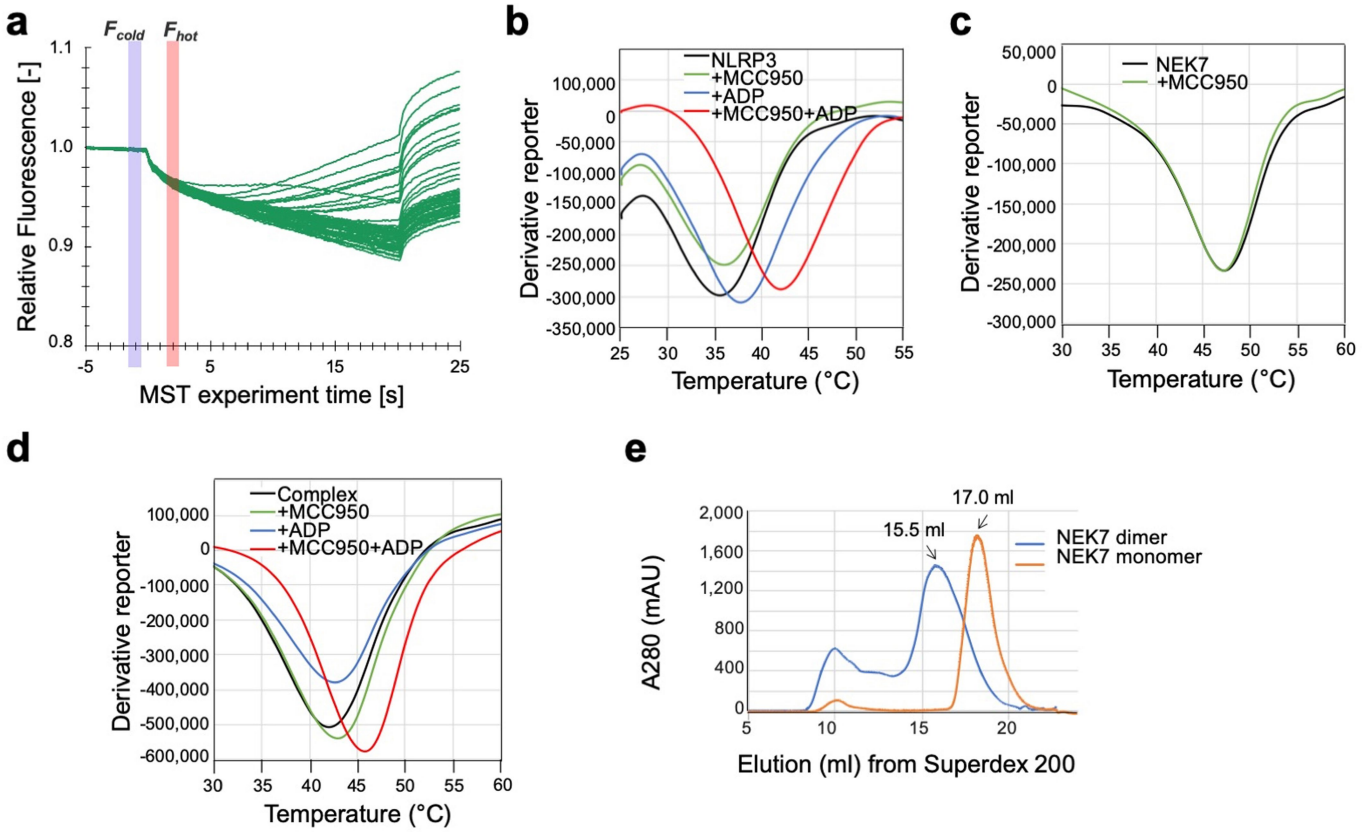

f

Sample	Superdex 200 Elution	MALS Mass	Calculated MW
NLRP3-NEK7 Monomer	12.6 ml	195.2 kDa	180 kDa
NLRP3/-NEK7 Dimer	11.5 ml	395.5 kDa	360 kDa

Extended Data Fig. 1 | NLRP3–NEK7 protein purification and characterization. a, Raw traces (of three independent replicates) of microscale thermophoresis measurements corresponding to titration of NEK7 against Alexa Fluor 488-labelled NLRP3. **b**–**d**, Representative thermal denaturation curves of NLRP3 (**b**), NEK7 (**c**) and complex (**d**), alone and in the presence of ADP and/or MCC950. The peak minima of the derivative curves correspond to the protein melting temperatures (T_m) (repeated $\geq$ 3 times). **e**, Gel filtration profile of wild-type NEK7 (monomer) and engineered NEK7 dimer on Superdex 200 column (repeated $\geq$ 5 times). **f**, Molecular masses of NLRP3–NEK7 dimer and monomer complexes, measured by in-line MALS.

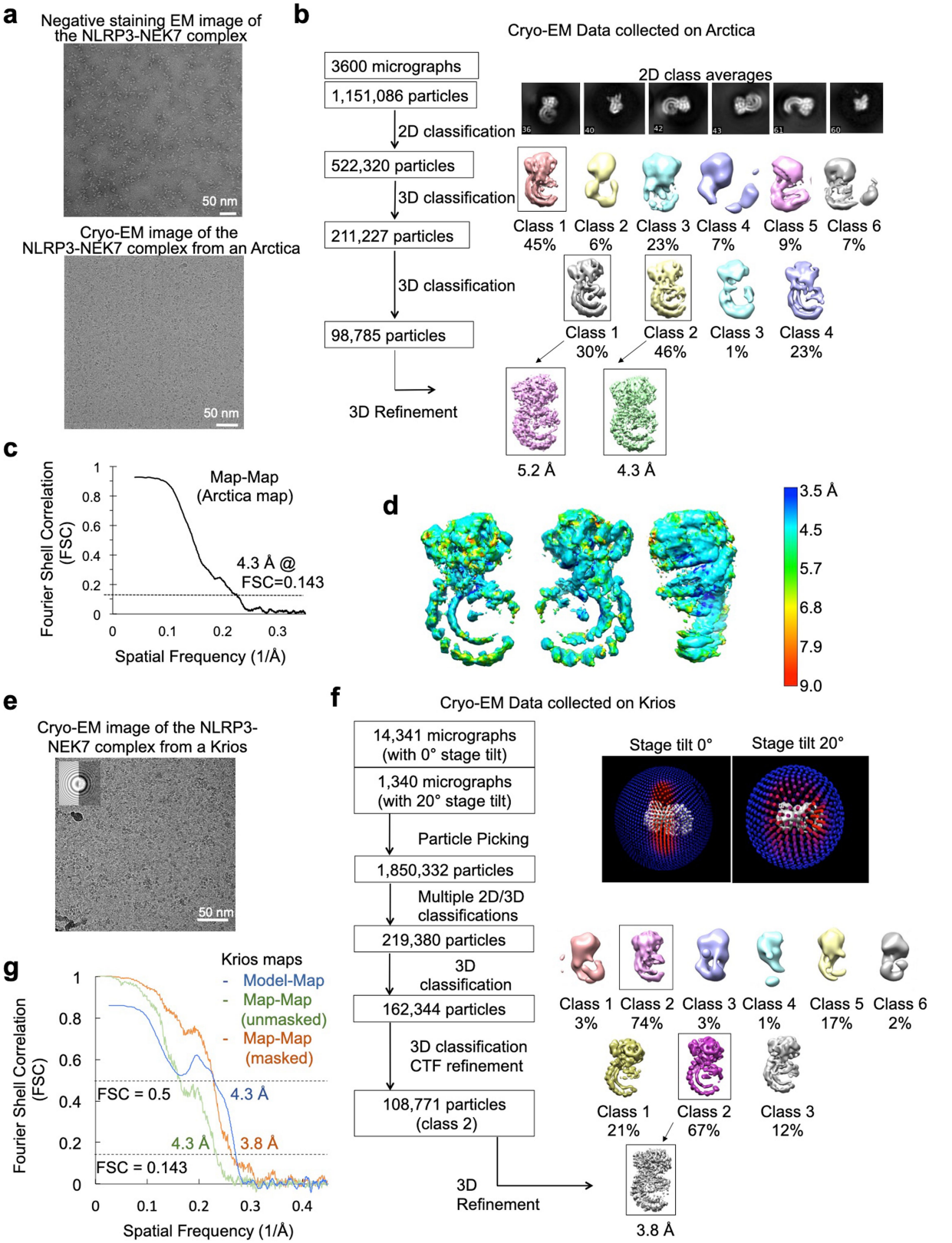

Extended Data Fig. 2 | Analysis and workflow for cryo-EM data collected on a Talos Arctica and on a Titan Krios. a, A negative-staining electron microscopy image (top, one among a few hundred images) and a cryo-EM micrograph (bottom, one among a few thousand images) of the NLRP3–NEK7 complex from a Talos Arctica. Scale bars, 50 nm. **b**, Workflow of cryo-EM data analysis of the Arctica data, performed in RELION 3.0[53] and cisTEM[46]. **c**, Gold-standard FSC curve between two half maps from the Arctica data. **d**, Local resolution estimation of the Arctica map generated by ResMap[41], coloured on the cryo-EM density (8σ). The highest resolution is observed where NEK7 interacts with NLRP3. **e**, A cryo-EM micrograph of the NLRP3–NEK7 complex from a Titan Krios (one among more than 10,000 images). Scale bar, 50 nm. The inset shows the modelled (left) and actual (right) Thon rings. **f**, Workflow of cryo-EM data analysis of the Krios data, done in RELION 3.0[53] and ROME 1.1[48]. The top right insets show the orientation distributions of the particles from the dataset of tilt 0° and tilt 20°. **g**, Gold-standard FSC curves between two half maps from the Krios data with mask (orange) and without mask (green), and between map and model (blue).

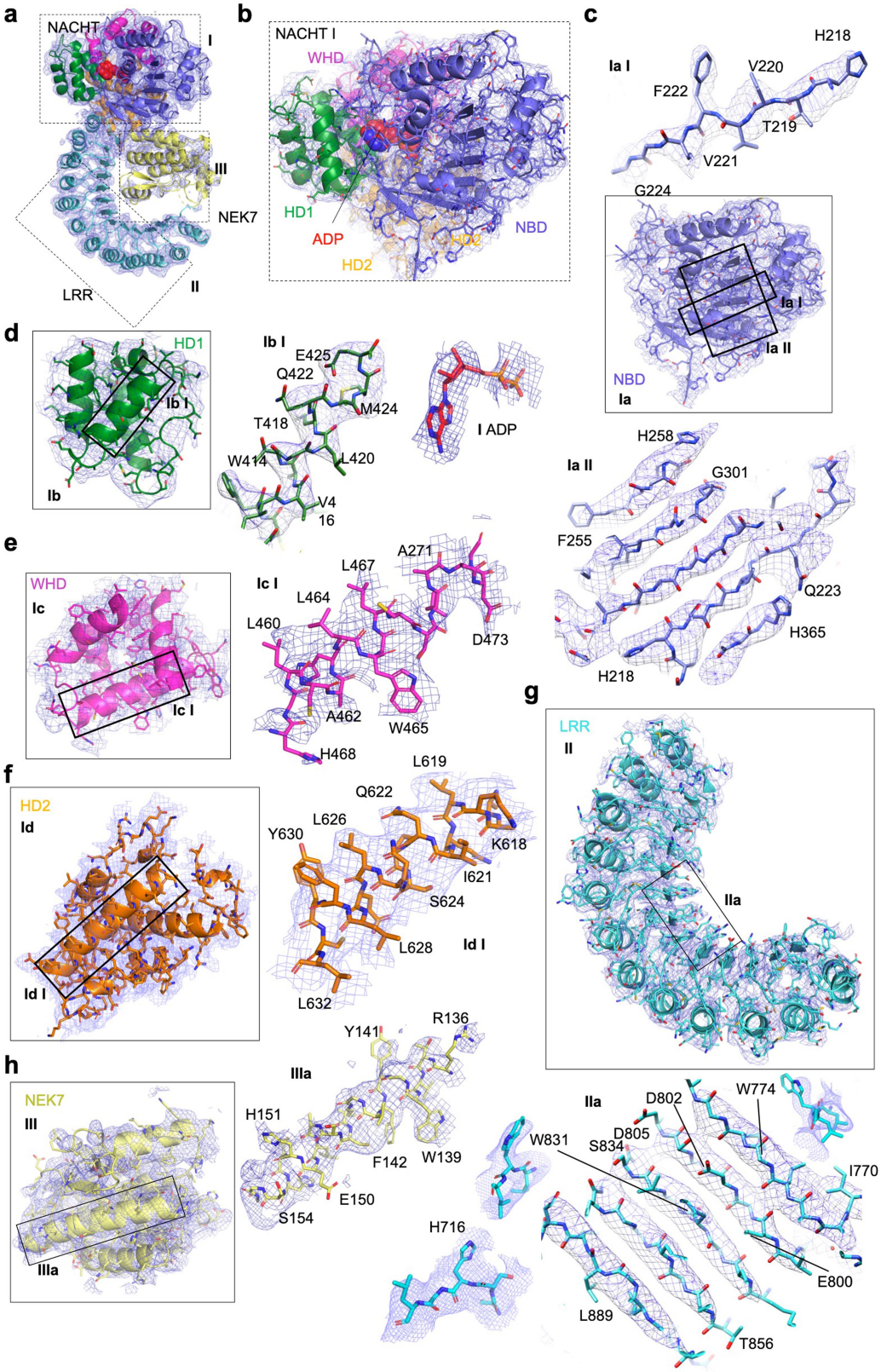

Extended Data Fig. 3 | Local density fitted with NLRP3 and NEK7. All magnified views are labelled with domain names and selected segment residue numbers. Densities are shown at 3σ.

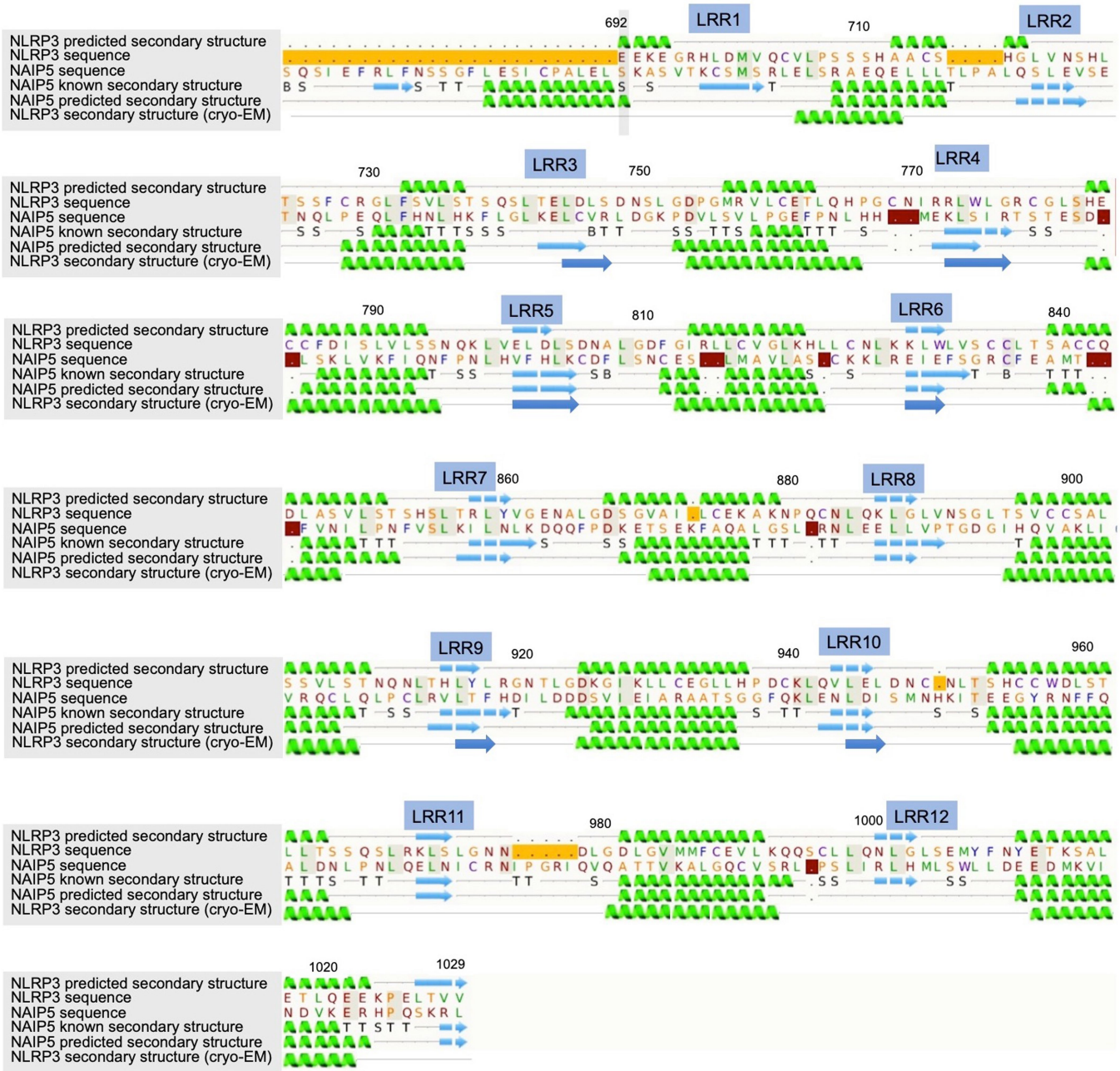

Extended Data Fig. 4 | Predicted and cryo-EM-derived secondary structures of the NLRP3–LRR domains aligned to NLRP3 and NAIP5 sequences. Twelve LRRs in NLRP3 were predicted by the Phyre2 server[24].

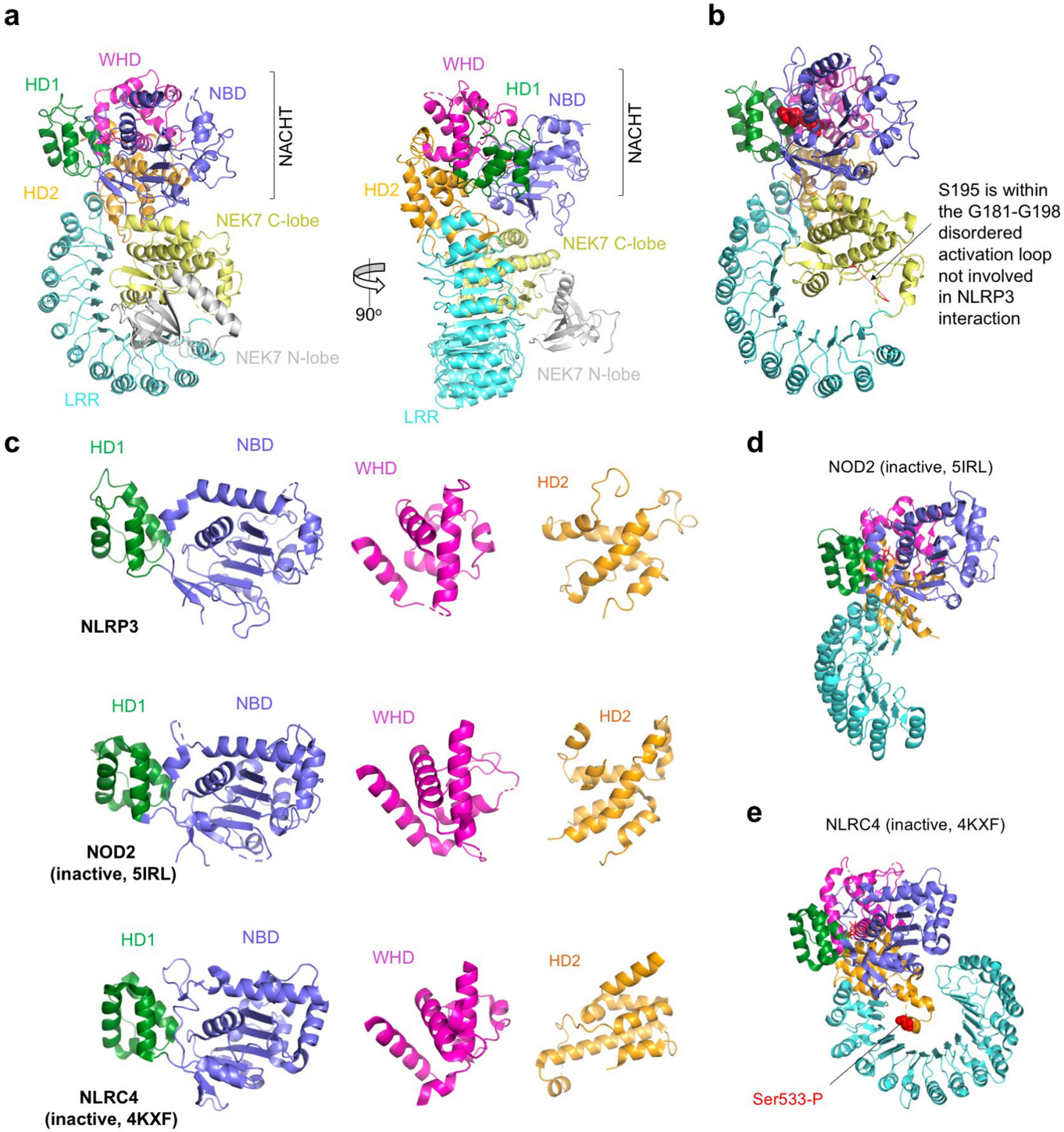

Extended Data Fig. 5 | The structure of the NLRP3–NEK7 complex, showing the modelled full-length NEK7 and NLRP3 domain comparisons. a, Two views of the NLRP3–NEK7 complex structure with the NEK7 N-lobe (grey) modelled from the NEK7 crystal structure (PDB code 2WQM). **b**, The disordered activation loop, including S195 in the NLRP3–NEK7 complex, which is not involved in NLRP3 interaction. **c**, NBD, HD1, WHD and HD2 of NLRP3, NOD2 (PDB code 5IRL) and NLRC4 (PDB code 4KXF) superimposed and shown side-by-side for comparison. **d**, **e**, NOD2 (**d**) and NLRC4 (**e**) structures[6,21] in inactive conformations and in the orientation of NLRP3 (shown in **a**) by superposing on the NBD and HD1 domains. The location of phosphorylated S533 of NLRC4 is labelled.

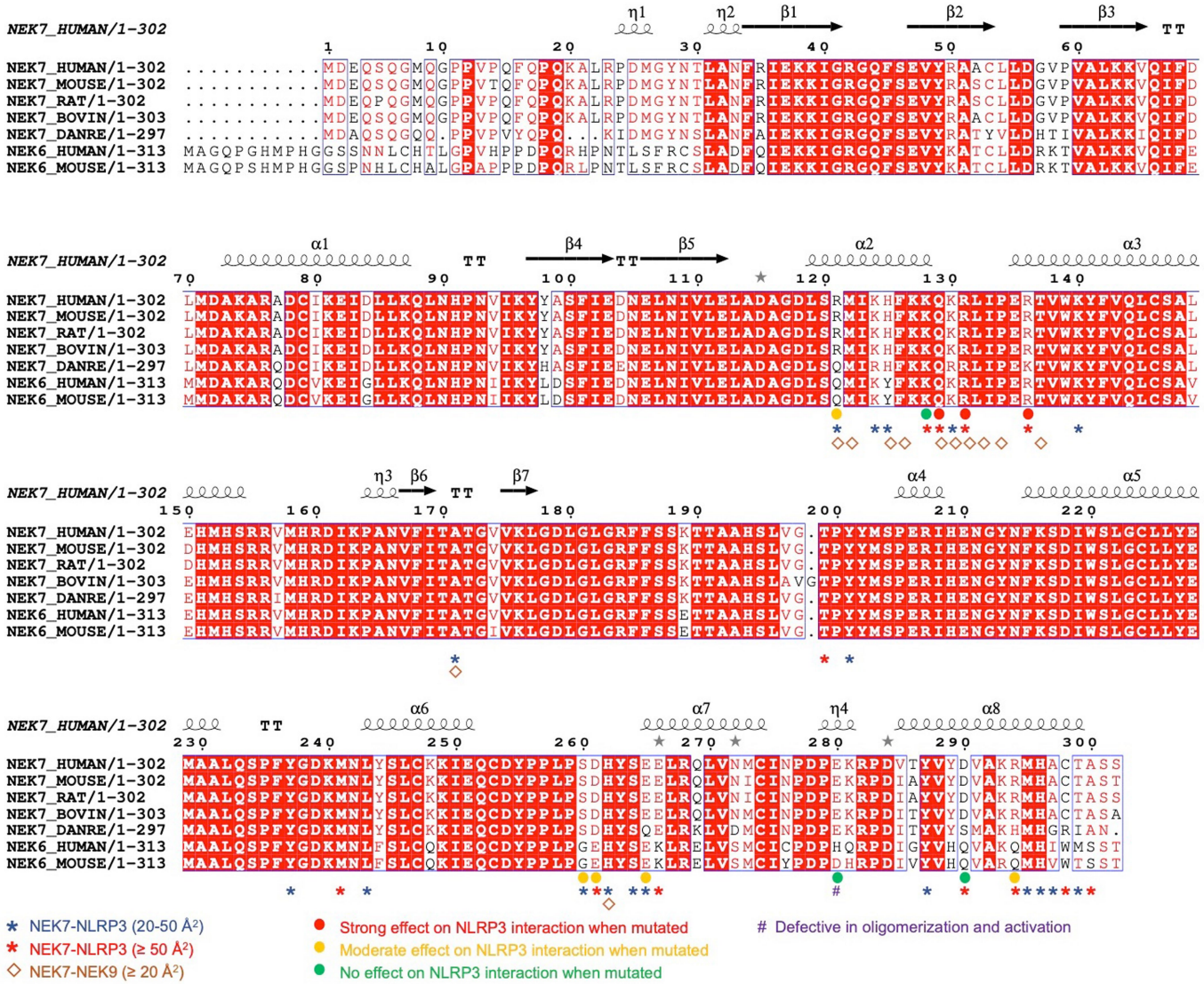

Extended Data Fig. 6 | Multiple sequence alignment of NEK7 and NEK6. Multiple sequence alignment was performed by the eScript server[54]. Annotations are based on the PISA server[28] analysis, and mutational data from Figs. 3, 4.

Extended Data Fig. 7 | Multiple sequence alignment of NLRP3. Multiple sequence alignment was performed by the eScript server[54]. Annotations are based on the PISA server[28] analysis, and mutational data from Figs. 3, 4.

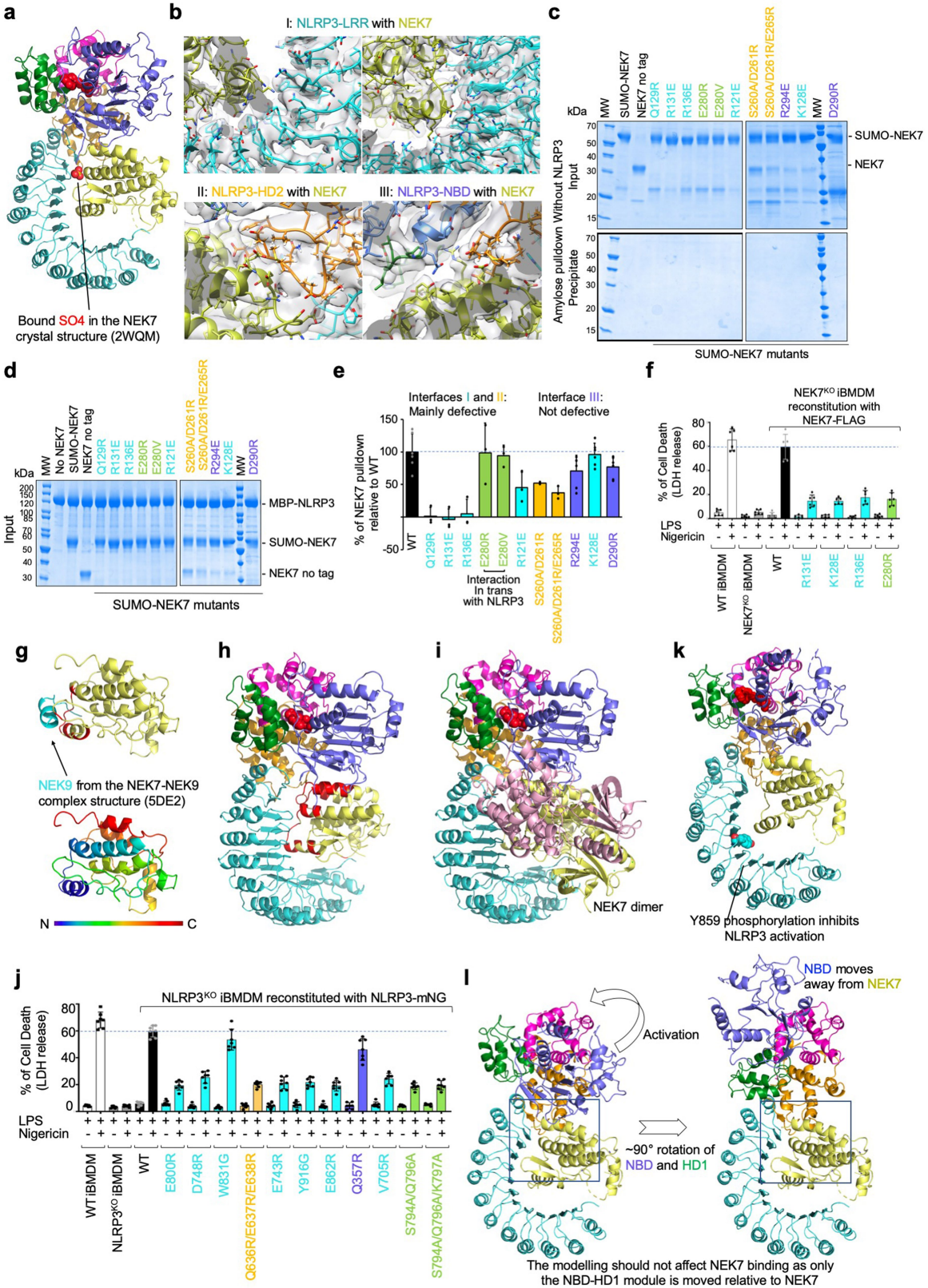

Extended Data Fig. 8 | See next page for caption.

Extended Data Fig. 8 | Structural analysis, mutagenesis tests and overlap between the NEK9- and NLRP3-binding sites on NEK7. **a**, Position of the bound SO_4 ion as in the NEK7 crystal structure[25], superimposed here in the structure of the NLRP3–NEK7 complex. **b**, Cryo-EM densities (5σ) at the NLRP3–NEK7 interfaces. Views correspond to those of Fig. 3b, c. **c**, Amylose pulldown of wild-type and mutant NEK7 without NLRP3, showing input and precipitate gels, which serve as negative controls for Fig. 3d. Experiments were repeated 3–6 times. **d**, Input gel for amylose pulldown of wild-type and mutant NEK7 shown in Fig. 3d. Experiments were repeated 3–6 times. **e**, Alternative calculation of the percentage of NEK7 pulldown relative to wild type, by subtracting the NEK7/NLRP3 ratio in the absence of NEK7 from the observed NEK7/NLRP3 ratio (shown as mean ± s.d. for $n = 3$–6 experiments). **f**, Cytoplasmic LDH released into the supernatant, quantified by comparison with total intracellular LDH of untreated cells (triton-X-lysed). Data are presented as mean ± s.d. for $n = 3$ replicates from 2 independent experiments. **g**, Top, mapping the NEK9-binding site onto the structure of the NEK7–NEK9 complex (PDB code 5DE2)[29]. NEK7 and NEK9 are shown in yellow and cyan, respectively, with the NEK9-binding residues of NEK7 highlighted in red. Bottom, a rainbow-coloured NEK7 structure showing that the NEK9-binding residues are from the first part of the NEK7 C-lobe. **h**, Mapping the NLRP3-binding site (red) onto NEK7 in the NLRP3–NEK7 structure. The NLRP3-binding site overlaps with the NEK9-binding site on NEK7. **i**, Superposition of NEK7 back-to-back dimer (yellow and pink) in the NEK7–NEK9 complex structure (PDB code 5DE2)[29] onto the NEK7 monomer in the NLRP3–NEK7 structure. The pink monomer in the NEK7 dimer clashes with NLRP3, which suggests that NEK7 dimerization cannot occur in the NLRP3–NEK7 complex. **j**, NLRP3-knockout iBMDMs were reconstituted with wild-type or mutant human mNG-tagged NLRP3, primed by LPS (4 h) and stimulated by nigericin (30 min). LDH release was analysed as in **f**. Dots, individual data points. Data are presented as mean ± s.d. for $n = 3$ replicates from 2 independent experiments. **k**, LRR phosphorylation at Y859[30], which might cause steric and charge repulsion with NEK7. **l**, NLRP3 activation model and NEK7 interactions. The hypothetical ~90° rotation of the NBD and HD1 of NLRP3 upon activation moves the NBD away from the NEK7 interaction region (indicated by a box).

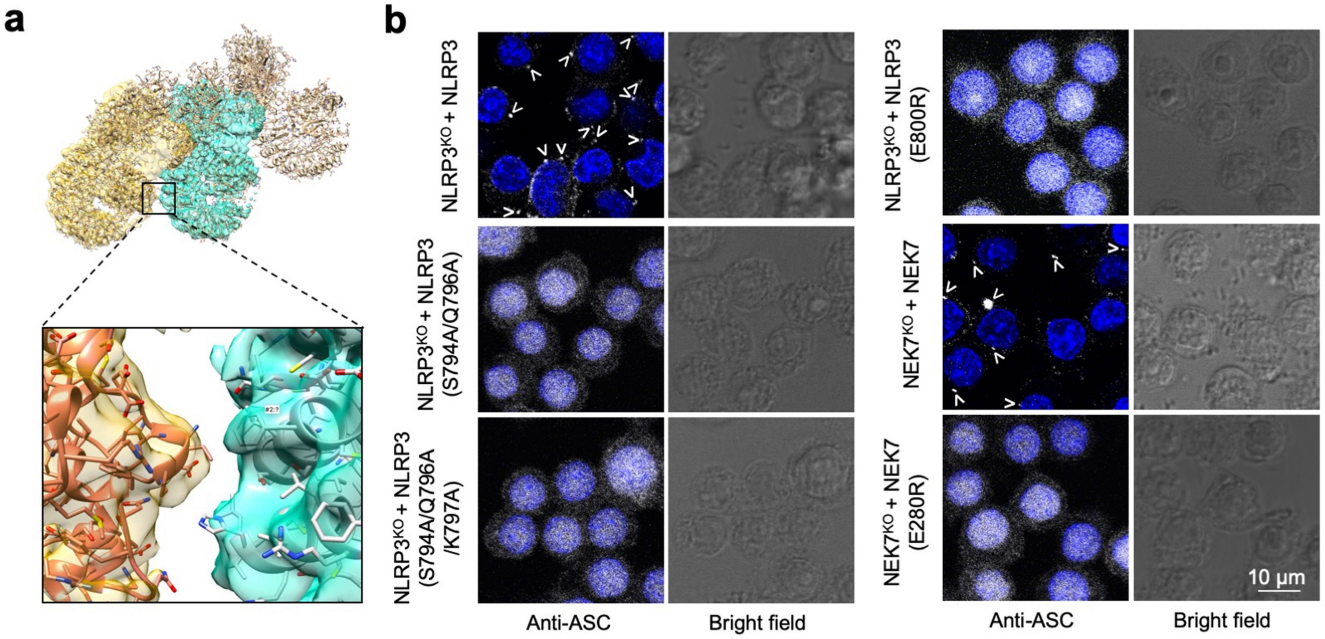

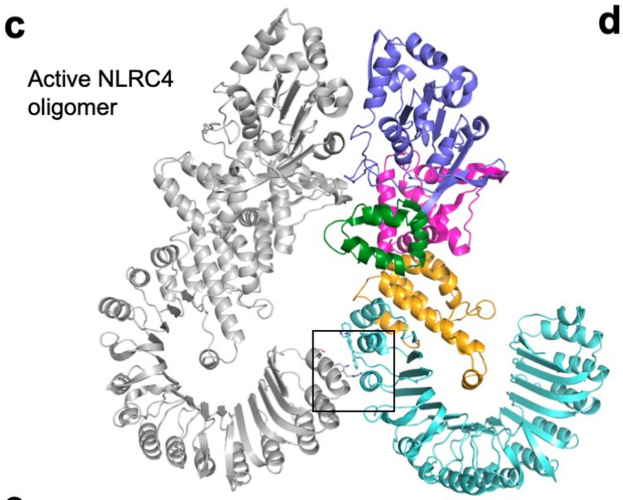

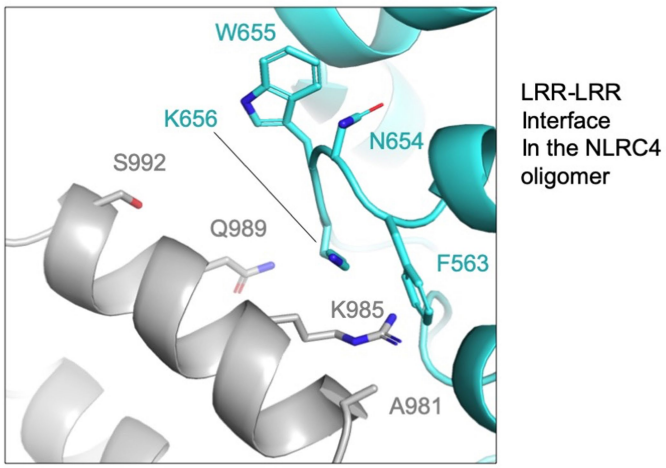

e

Human NLRP3	Mouse NLRP3	Disease	Domain	Structural effect	PISA analysis
Arg260Trp, Leu, Pro	Arg258	Muckle-Wells Syndrome	NBD	WHD interaction	Buried
Leu264Pro	Leu262	CINCA/NOMID Syndrome	NBD	WHD interaction	Partially buried
Asp303Asn, Gly	Asp301	CINCA/NOMID Syndrome	NBD	HD2 interaction – Walker B	Partially buried
Glu304Lys	Glu302	CINCA/NOMID Syndrome	NBD	ADP/ATP binding – Walker B	Partially buried
Leu305Pro	Leu303	FCAS	NBD	Local conformation	Buried
Thr348Met	Thr346	Muckle-Wells Syndrome	NBD	Local conformation	Buried
Ala352Val	Ala350	Muckle-Wells Syndrome	NBD	HD2 interaction	Buried
Thr436Ile	Thr434	CINCA/NOMID Syndrome	HD1	HD2 interaction	Partially buried
Ala439Val	Ala437	FCAS	WHD	HD1 interaction	Buried
Phe523Cys	Phe523	Muckle-Wells Syndrome	WHD	Local conformation	Buried
Gly569Ala	Gly569	Muckle-Wells Syndrome	HD2	WHD interaction	Buried
Glu627Gly	Glu627	FCAS	HD2	Local conformation	Partially buried
Met659Lys	Met659	FCAS	HD2	Disordered	Disordered
Gly755Arg, Ala	Gly754	CINCA/NOMID Syndrome	LRR	NEK7 binding enhancement	Partially buried

Extended Data Fig. 9 | See next page for caption.

Extended Data Fig. 9 | NLRP3–NEK7 interaction *in trans* and NLRP3 CAPS mutations. a, Cryo-EM density (5σ) fitted to the oligomeric model, zoomed in at an NLRP3–NEK7 interface *in trans*. **b**, Immunofluorescence imaging for assessing ASC speck formation. NLRP3-knockout and NEK7-knockout iBMDMs were reconstituted with wild-type and mutant constructs as depicted. ASC speck formation upon nigericin activation was analysed by anti-ASC antibody. Nucleus was stained by Hoechst 33342. Scale bar, 10 μm. Images are representative of two independent experiments. **c**, An active NLRC4 oligomer structure[20] shown for the LRR–LRR interaction. **d**, Magnified view showing the detailed LRR–LRR interaction *in trans* boxed in **c**. **e**, Mapping of pathogenic disease mutations onto the NLRP3 structure. CAPS-associated pathogenic mutations derived from the Infevers database[33] are shown with their predicted effect, based on the NLRP3 structure. Green, disruption of inter-domain interactions in the inactive conformation; mauve, change of local conformation by mutating residues buried within the domains; yellow, alteration in key residues in the Walker B motif; grey, enhancement of NEK7 binding. CINCA, chronic infantile neurological cutaneous articular; NOMID, neonatal-onset multisystem inflammatory disorder; FCAS, familial cold auto-inflammatory syndrome.

Extended Data Table 1 | Cryo-EM data collection, refinement and validation statistics

	NLRP3-NEK7 Talos Arctica dataset	NLRP3-NEK7 Titan Krios dataset
Data collection and processing		
Magnification	105,000	165,000
Voltage (keV)	200	300
Electron exposure (e–/Å^2)	~59	~55
Defocus range (μm)	-0.5 to -3.0	-0.8 to -3.0
Super Resolution pixel size (Å)	0.589	0.42
Symmetry imposed	C1	C1
Initial particle images (no.)	1,086,055	1,850,332
Final particle images (no.)	98,340	108,771
Map resolution (Å)	4.3	3.8
FSC threshold	0.143	0.143
Map resolution range (Å)	3.5-5.8	2.5-6.6
Refinement		
Initial model used		
Model resolution (Å)		4.3
FSC threshold		0.5
Model resolution range (Å)		2.5-6.6
Map sharpening *B* factor (Å^2)		-100
Model composition		
Non-hydrogen atoms		7979
Protein residues		980
Ligands		1
B factors (Å^2)		
Protein		132.7
Ligand		96.7
R.m.s. deviations		
Bond lengths (Å)		0.006
Bond angles (°)		1.345
Validation		
MolProbity score		2.35
Clashscore		8.92
Poor rotamers (%)		1.91
Ramachandran plot		
Favoured (%)		84.96
Allowed (%)		14.02
Disallowed (%)		1.02

nature research

Corresponding author(s): Hao Wu, Youdong Mao

Reporting Summary

Nature Research wishes to improve the reproducibility of the work that we publish. This form provides structure for consistency and transparency in reporting. For further information on Nature Research policies, see Authors & Referees and the Editorial Policy Checklist.

Statistical parameters

When statistical analyses are reported, confirm that the following items are present in the relevant location (e.g. figure legend, table legend, main text, or Methods section).

n/a	Confirmed	
☐	☒	The exact sample size (*n*) for each experimental group/condition, given as a discrete number and unit of measurement
☐	☒	An indication of whether measurements were taken from distinct samples or whether the same sample was measured repeatedly
☐	☒	The statistical test(s) used AND whether they are one- or two-sided *Only common tests should be described solely by name; describe more complex techniques in the Methods section.*
☒	☐	A description of all covariates tested
☐	☒	A description of any assumptions or corrections, such as tests of normality and adjustment for multiple comparisons
☒	☐	A full description of the statistics including central tendency (e.g. means) or other basic estimates (e.g. regression coefficient) AND variation (e.g. standard deviation) or associated estimates of uncertainty (e.g. confidence intervals)
☒	☐	For null hypothesis testing, the test statistic (e.g. *F*, *t*, *r*) with confidence intervals, effect sizes, degrees of freedom and *P* value noted *Give P values as exact values whenever suitable.*
☒	☐	For Bayesian analysis, information on the choice of priors and Markov chain Monte Carlo settings
☒	☐	For hierarchical and complex designs, identification of the appropriate level for tests and full reporting of outcomes
☒	☐	Estimates of effect sizes (e.g. Cohen's *d*, Pearson's *r*), indicating how they were calculated
☐	☒	Clearly defined error bars *State explicitly what error bars represent (e.g. SD, SE, CI)*

Our web collection on statistics for biologists may be useful.

Software and code

Policy information about availability of computer code

Data collection	Cryo-EM data was carried out with SerialEM 3.7
Data analysis	Microscale Thermophoresis data analysis was done with MO Control software provided by (NanoTemper, Munich, Germany) Multi-angle light scattering (MALS) data analysis was carried out using ASTRA V Cryo-EM data analysis was done with MotionCor2, CTFFIND4, RELION 3.0, cisTEM 1.0.0., Gautomatch v0.56, Gctf v1.18, ROME 1.1.2 package, Coot-0.8.9.2, Chimera1.13.1, Pymol 2.3.1 Phyre2 server http://www.sbg.bio.ic.ac.uk/phyre2/html/page.cgi?id=index Thermal Shift assay data was analyzed with Protein Thermal ShiftTM Software (Thermo Fisher Scientific) Adobe Photoshop software for image processing Statistical analysis were performed using MS Excel and GraphPad Prism 7 All references are given in the Material and Methods section

For manuscripts utilizing custom algorithms or software that are central to the research but not yet described in published literature, software must be made available to editors/reviewers upon request. We strongly encourage code deposition in a community repository (e.g. GitHub). See the Nature Research guidelines for submitting code & software for further information.

Data

Policy information about availability of data

All manuscripts must include a data availability statement. This statement should provide the following information, where applicable:

- Accession codes, unique identifiers, or web links for publicly available datasets
- A list of figures that have associated raw data
- A description of any restrictions on data availability

The cryo-EM map has been deposited in the Electron Microscopy Data Bank under the accession number EMD-0476. The atomic coordinates have been deposited in the Protein Data Bank under the accession number 6NPY.

Field-specific reporting

Please select the best fit for your research. If you are not sure, read the appropriate sections before making your selection.

☒ Life sciences ☐ Behavioural & social sciences ☐ Ecological, evolutionary & environmental sciences

For a reference copy of the document with all sections, see nature.com/authors/policies/ReportingSummary-flat.pdf

Life sciences study design

All studies must disclose on these points even when the disclosure is negative.

Sample size	No statistical methods were used to predetermine sample sizes.
Data exclusions	No data were excluded.
Replication	All experiments were confirmed with multiple biological replicates as detailed in Methods or Figure Legends
Randomization	No randomization was performed.
Blinding	No blinding is used.

Reporting for specific materials, systems and methods

Materials & experimental systems

n/a	Involved in the study
☐	☒ Unique biological materials
☐	☒ Antibodies
☐	☒ Eukaryotic cell lines
☒	☐ Palaeontology
☒	☐ Animals and other organisms
☒	☐ Human research participants

Methods

n/a	Involved in the study
☒	☐ ChIP-seq
☒	☐ Flow cytometry
☒	☐ MRI-based neuroimaging

Unique biological materials

Policy information about availability of materials

Obtaining unique materials	All data can be obtained from the corresponding author upon reasonable request.

Antibodies

Antibodies used	anti-human NLRP3 antibody (Adipogen, Cat no: AG-20B-0014-C100), anti-mouse caspase-1 antibody (Adipogen, Cat. no: AG-20B-0042-C100), anti-FLAG F1804-Sigma, Anti-NEK7 antibody [EPR4900] Abcam, anti-ASC Cell Signaling Technology, Cat. no: 67824S, Goat anti-rabbit (H+L) Alexa Fluor 647 conjugated, Thermo Fischer Scientific, Cat. no: A- 21245, Anti-β-actin (mouse monoclonal, Santa Cruz Biotechnology, Cat. no: 47778)

Validation	All the commercial antibodies were verified by the manufacturers according to immunoblots and/or images on their websites.

Eukaryotic cell lines

Policy information about cell lines

Cell line source(s)	NLRP3 KO iBMDM was a kind gift by Kate Fitzgerald and NEK7 KO iBMDM by Gabreil Nunez HEK293T (ATCC) https://www.atcc.org/en/Products/All/CRL-3216.aspx SF9 cells from Thermo Fischer Scientific https://www.thermofisher.com/order/catalog/product/11496015 BL21(DE3) from Agilent https://www.agilent.com/en/product/protein-expression/competent-cells-for-routine-protein-expression/general-protein-expression/bl21(de3)-competent-cells-232943
Authentication	Cell lines were verified by manufacturer's website and Identity of these cell lines were frequently checked by their morphological features HEK293T (ATCC) https://www.atcc.org/en/Products/All/CRL-3216.aspx SF9 cells from Thermo Fischer Scientific https://www.thermofisher.com/order/catalog/product/11496015 BL21(DE3) from Agilent https://www.agilent.com/en/product/protein-expression/competent-cells-for-routine-protein-expression/general-protein-expression/bl21(de3)-competent-cells-232943
Mycoplasma contamination	All cell lines were tested to be mycoplasma-negative by PCR.
Commonly misidentified lines (See ICLAC register)	No commonly misidentified cell lines are used in this study.